Experimental Application of a Quasi-Static Adaptive Controller to a Dual Independent Swirl Combustor

Juan A. Paredes, Rahul Ramesh, Mirko Gamba & Dennis S. Bernstein

Published online: 08 Feb 2024.

Submit your article to this journal

Article views: 22

View related articles

View Crossmark data

Taylor & Francis
Taylor & Francis Group

Check for updates

Experimental Application of a Quasi-Static Adaptive Controller to a Dual Independent Swirl Combustor

Juan A. Paredes, Rahul Ramesh, Mirko Gamba, and Dennis S. Bernstein

Department of Aerospace Engineering, University of Michigan, Ann Arbor, Michigan, USA

ABSTRACT

Thermoacoustic instabilities in gas turbine combustors have multiple detrimental effects. Although active control techniques can mitigate these instabilities, high-bandwidth actuators are typically needed. The present work develops an adaptive feedback-control technique that operates with actuators that have low bandwidth relative to the dynamics of the combustor. This technique, which is an extension of retrospective cost adaptive control (RCAC) that accounts for the actuator bandwidth limitation, is called quasi-static RCAC (QSRCAC). QSRCAC uses a Kalman filter to estimate the gradients of the performance variables, which are then used as directions of search to determine the next actuator commands that minimize user-defined performance metrics. It is applied to the Dual Independent Swirl Combustor (DISCo), a methane/air gas turbine model combustor which has multiple dominant instability modes above 250 Hz and whose mass flow control inputs operate at a significantly lower bandwidth of 5 Hz. Single and multiple objective control scenarios such as minimizing thermoacoustic oscillations while maintaining a user-defined temperature at the exit of the combustor are studied. Experimental results show that QSRCAC minimizes thermoacoustic oscillations successfully in all cases. In the multi-objective scenarios, when complementary objectives are presented, such as minimizing thermoacoustic instabilities and increasing the exit temperature, QSRCAC achieves both objectives; when presented with multiple contrasting objectives, such as minimizing thermoacoustic instabilities and diminishing the exit temperature, QSRCAC minimizes thermoacoustic oscillations with higher priority.

Introduction

Gas turbines are a primary source of power generation in both aircraft and land-based systems. In such a multiplex system, power and efficiency is dependent on turbomachinery such as the compressor, turbine modules and a combustion device. The combustion chamber plays a crucial role in determining the highest temperature reached in the cycle (firing temperature), NOx generation, and net power output of a gas turbine engine, motivating the present work. While traditional combustor architectures based on diffusion combustion, such as rich-quench-lean combustion (Feitelberg and Lacey 1998; Samuelsen 2006) produce highly stable and flashback-free operation of the combustor, these fail to meet evolving emission regulations, especially NOx (Gupta 1997). Since reducing fuel burn

CONTACT Juan A. Paredes ✉ jparedes@umich.edu 🖂 Department of Aerospace Engineering, University of Michigan, Ann Arbor, Michigan, USA

and avoiding higher temperatures reduces NOx formation, the industry has adopted lean combustion (McDonell 2016). Lean combustion, however, is prone to combustion instabilities. The underlying mechanism responsible for these instabilities involves a combination of convective and acoustic dynamics, each supported by and coupled to the dynamics of the turbulent flowfield, turbulence-chemistry interactions, and the acoustic properties of the combustor (Keller 1995; Lieuwen 2003, 2012; Zinn and Lieuwen 2005). These instabilities cause large-amplitude pressure oscillations of the flowfield, which may result in flameout, thermal NOx growth, thermal cycling, structural fatigue, and combustion efficiency reduction, which can negatively impact the performance and structural integrity of the system.

Various methodologies such as passive and active control have been proposed for mitigating thermoacoustic oscillations in gas turbine combustors. Passive control techniques seek to prevent or reduce these oscillations by redesigning the hardware of the combustor, such as the fuel and air injectors or the combustor geometry, and placing acoustic dampers such as acoustic liners and Helmholtz resonators as shown in Gysling et al. (1999); Pan et al. (2020); Richards, Straub, and Robey (2003); Sohn and Park (2011); Zhao et al. (2009); Zhao, Gutmark, and Reinecke (2019); Zhao and Li (2015). Such modifications involve high costs and at best extend the range of operation by a limited amount (Dowling and Morgans 2005a). Furthermore, operating point changes for meeting load demand and fuel variations may move the operation toward thermoacoustic instabilities. In contrast, active open/closed-loop control techniques use actuators such as fuel/air injectors and loudspeakers to dampen the instabilities. Active open-loop control strategies do not require feedback from sensors and can be implemented with low-bandwidth actuators; these open-loop strategies include periodic fuel injection Hathout, Fleifil, Annaswamy and Ghoniem (2002), high-momentum air jet modulation (Uhm and Acharya 2005, 2006), radial air injection (Deshmukh and Sharma 2017), and periodic acoustic forcing (Guan et al. 2019). However, these do not possess the ability to react to significant changes in the combustor dynamics during operation, in contrast to active closed-loop control strategies.

Active closed-loop (feedback) control techniques seek to suppress thermoacoustic instabilities by modulating actuators using data from sensors, such as pressure and chemiluminescence measurements, thereby stabilizing the commanded operating point as it changes, as reported in Annaswamy and Ghoniem (2002); Brunton and Noack (2015); Dowling and Morgans (2005b); McManus, Poinsot, and Candel (1993); Mongia et al. (2003). These closed-loop strategies include phase-shift control (de Andrade, Vazquez, and Pagano 2017; Heckl 1988; Zalluhoglu, Kammer, and Olgac 2016), linear – quadratic – Gaussian (LQG) control (Chen, Fathy, and O'Connor 2020), adaptive control based on dynamic compensation (Wei et al. 2013), and backstepping-based control (Aarabi, Ghadiri-Modarres, and Mojiri 2023). Since thermoacoustic oscillations typically occur at high frequency (greater than 100 Hz), active feedback controllers require also high bandwidth actuators (Yi and Gutmark 2007; Zhao et al. 2018). This requirement can be prohibitive as such actuators control relatively small flow rates and cannot operate in harsh environments.

Another approach to low-bandwidth feedback control is operating point control (OPC), where sensor data are used to search for an operating point that optimizes a performance metric (Docquier and Candel 2002). This approach includes strategies such as equivalence ratio modulation, as shown in Ding et al. (2019); Docquier, Lacas, and Candel (2002); Richards, Janus, and Robey (1999). As mentioned in Krishnamoorthy and Skogestad

(2022), the approach is similar to real-time optimization techniques since, under slow actuator modulation, the plant dynamics can be represented as a static map. Henceforth, we refer to these techniques as *quasi-static control*. The present work considers quasi-static RCAC (QSRCAC), an extension of retrospective cost adaptive control (RCAC) (Islam et al. 2021; Rahman, Xie, and Bernstein 2017).

The main contribution of the present work is the development and experimental implementation of a novel version of QSRCAC. RCAC has been previously implemented for active feedback control of thermoacoustic instabilities in a Rijke-tube experiment using high-bandwidth actuators (Paredes and Bernstein 2023; Paredes, Islam, and Bernstein 2022). QSRCAC constitutes an extension of RCAC that facilitates implementation on systems with low-bandwidth actuators. A preliminary version of QSRCAC was considered in Bruce et al. (2020) and in our previous work Paredes et al. (2022). The present work constitutes a major expansion by replacing the gradient estimation technique in Paredes et al. (2022) with the technique featured in Gelbert et al. (2012) with application to a combustion device.

We apply and demonstrate QSRCAC in our Dual Independent Swirl Combustor (DISCo), which is a laboratory scale gas turbine model combustor. Our previous work Paredes et al. (2022) focused on achieving the single objective of reducing the pressure oscillations in DISCo. We now increase the scope of the control problem to include a second control objective of achieving a desired net power output. In a typical gas turbine, the power output increases (decreases) as firing temperature in the combustion chamber is increased (decreased) when all other variables are kept constant. Hence, the present work extends the applications of QSRCAC and Paredes et al. (2022) to include a user-defined firing temperature as an additional objective that serves as a surrogate for controlling the net power output of the device.

The objectives are encoded into nonnegative performance variables, such as minimizing the root-mean-square (RMS) of pressure oscillations measured in the combustion chamber and the squared difference between a desired and measured temperatures. In combination, this results in the mitigation of thermoacoustic oscillations and reaching a user-defined combustor exit (firing) temperature goal, respectively. The firing temperature goal chosen to mimic a change in net power output could be higher or lower than the value measured at the initial operating point. While QSRCAC focuses on two such objectives, neither stoichiometric or lean combustion conditions close to the lean blowout limit are explicitly sought in the present work.

A crucial aspect of QSRCAC is the selection of hyperparameters, which determine the rate of adaptation, the controller order, and the controller performance, and must be selected before actual laboratory tests. While this can be achieved by running several closed-loop tests in the combustor and iterating through several combinations of hyperparameters, this can be both time consuming and resource intensive. Hence, a mathematical representation of the combustor response to a given set of input variables is developed empirically and later used in closed-loop simulation tests to enable a resource efficient hyperparameter selection procedure.

The specific technical contributions of the present work are summarized below:

i) Development of a novel version of QSRAC suitable for application to quasi-static control of a laboratory-scale gas turbine model combustor;

ii) Development of a design of experiments (DoE) based offline simulation model of a combustor that enables a controller-hyperparameter tuning at a low resource cost;

iii) Application of QSRCAC to DISCo with multiple objectives, which include minimizing thermoacoustic oscillations and maintaining a user-defined firing temperature at the exit of the combustor while satisfying input constraints with operation between the lean blowout limit and stoichiometric conditions.

The contents of the paper are as follows. Section 2 provides an overview of DISCo. Section 3 provides an overview of the the QSRCAC algorithm. Section 4 specifies the control problem and describes the experimental operating conditions of DISCo for the laboratory experiments. Section 5 presents the DoE based offline simulation model of DISCo and the numerical simulations used for QSRCAC hyperparameter selection. Section 6 presents the DISCo laboratory experiments performed with QSRCAC using the hyperparameters selected in Section 5 and provides a discussion of the results. Finally, Section 7 presents conclusions.

Overview of DISCo

This section provides a brief description of DISCo, shown in Figure 1. DISCo is a laboratory-scale gas turbine model combustor designed to achieve thermal powers up to 40 kW using methane/air mixtures at atmospheric conditions while exciting thermoacoustic oscillations near 300 Hz. The novel dual swirler in DISCo allows for independent manipulation of the mass flow rate through each of the five flow paths labeled in Figure 1. The outer swirler (A) and inner swirler (B) are the primary air feeds associated with the outer swirler and inner swirler air mass flow rates, $\dot{m}_o, \dot{m}_i \in \mathbb{R}$, respectively. Furthermore, there exist secondary air feeds that sidestep the swirl vanes and contain only axial components for the inner swirler (C) and outer swirler (D). The fuel (methane) is supplied through a single feed (E), delivering a partially premixed mixture into the combustion chamber, associated with the fuel mass flow rate $\dot{m}_f \in \mathbb{R}$. Manipulation of
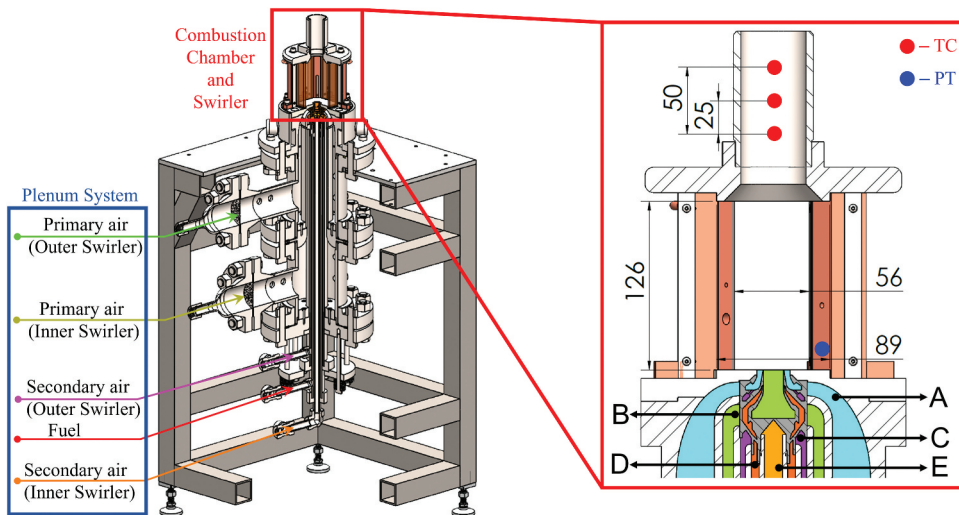

Figure 1. Three-dimensional rendering of DISCo and zoomed-in view of dual swirler flow paths and combustion chamber. Red and blue dots represent thermocouples (TC) and pressure sensors (PT). All dimensions are in mm.

these mass flow rates allows the users to independently vary the total air mass flow rate $\dot{m}_t \triangleq \dot{m}_i + \dot{m}_o$, fuel-air equivalence ratio $\phi \triangleq (\dot{m}_f/\dot{m}_t)/(\dot{m}_f/\dot{m}_t)_{st}$, where $(\dot{m}_f/\dot{m}_t)_{st}$ is the stoichiometric fuel-to-air ratio, outer-to-inner swirler split ratio $R \triangleq \dot{m}_o/\dot{m}_i$, and the swirl number of the inner and outer swirlers. The inner and outer swirl numbers in the base design with no axial air injection are $S_i = 0.75$ and $S_o = 1.1$, respectively. In its full capacity, DISCo can process a maximum air mass flow rate of 12 g/s in each swirler (inner and outer) while operating at equivalence ratios (ϕ) between 0.6 and 1.1. Regulation of the mass flow rates through each flow path is performed through five independent flow metering systems composed of choked orifices positioned downstream of dome pressure regulators controlled by electronic pressure controllers.

The combustor is operated by two control systems namely the main control system (MCS) and the secondary adaptive control system (SACS). The MCS acts as a supervisory control system that performs operations such as ignition, steady-state operation, shutdown and emergency operations, but does not perform any closed-loop stabilization operations. In a typical experiment, the MCS steers the combustor to an initial operating point after which the control of the mass flow regulators is transferred to the SACS, which implements QSRCAC in the DISCo laboratory experiments. The MCS is composed of a custom build data acquisition and control system based on National Instruments PCIe-6343 and PCIe-6346 multifunction I/O modules, while SACS is composed of a dSpace Scalexio digital computer, and digital-to-analog (D/A) and analog-to-digital (A/D) interfaces. Due to their distinct functions, the MCS and SACS acquire and process the data from the combustor at different rates.

The combustion chamber has a polygonal (octagonal) cross-section, it is 126 mm tall and terminates into a constant area exit chimney 127 mm in length. It is instrumented with a high intensity microphone (Kulite MIC-190 L) sampled at a frequency of 16 kHz by the MCS as shown in Figure 1. Bare wire type B thermocouples of 0.25 mm diameter are used to measure the temperature in the chimney of the combustor. A custom built electronic box amplifies the thermocouple signal by a factor of 500. The arrangement is calibrated up to 1000 K with an accuracy of $< 2\%$ and the results are extrapolated to higher temperatures. These thermocouples are sampled by the MCS at a frequency of 200 Hz and their position in the chimney is shown in Figure 1. The firing temperature is then computed as the average of the temperatures measured using the three such thermocouples separated by 50 mm. The SACS system uses the same pressure and temperature measurements listed above and the details of signal acquisition and processing are provided in Subsection 5.2.

A detailed thermoacoustic response of DISCo was presented in Ramesh et al. (2021) and Ramesh and Gamba (2022). It was shown that DISCo can excite multiple modes (longitudinal or Helmholtz modes) based on ϕ and R for specific fuel and air mass flow rates. As an example, Figure 2a shows the pressure fluctuation measured by the microphone located in the combustion chamber for the base operating point: $\dot{m}_t = 8$ g/s, $\phi = 0.85$ and $R = 1.6$. An amplitude spectral density (ASD) plot is then constructed by performing a fast Fourier transform (FFT) of the time-resolved pressure data; the resulting ASD plot is shown in Figure 2b, which displays two sharp peaks at 277 Hz and 553 Hz that can be attributed to the quarter wave mode of the inner swirl plenum and the longitudinal mode of the outer swirl plenum, respectively.
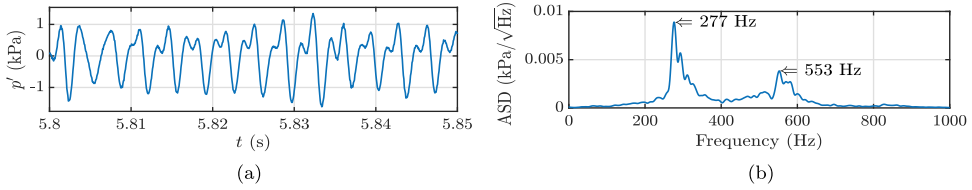
Figure 2. Example of frequency content of DISCo for operation at $\dot{m}_t = 8$ g/s, $\phi = 0.85$ and $R = 1.6$: (a) pressure fluctuation measured in the combustion chamber, and (b) corresponding ASD.

The influence of air split ratio (R) on combustion instabilities was studied in Ramesh and Gamba (2022) using particle image velocimetry and chemiluminescence imaging. Parametric variations in R and ϕ space were performed for $\dot{m}_t = 8$ g/s with variations in $R \in [0.5, 4]$ and $\phi \in [0.7, 1]$ in increments of 0.5 and 0.1 respectively. It was shown that the base operating point has a critical value of R that produces a flat compact flame. This results in the amplification of the longitudinal acoustic mode as the entire flame has nearly the same convective time scale and a high amplitude of pressure fluctuations. However, as R is decreased or increased from the base operating condition, the flame structure becomes more distributed and V-shaped. In such a flame, the heat release occurs at points with differing convective time scales resulting in the suppression of the longitudinal mode observed in the previous case. However, the Helmholtz modes of different elements are excited at different split ratios. In such cases, significantly lower amplitude pressure fluctuations are observed compared to the flat compact flame.

Overview of quasi-static retrospective cost adaptive control

An overview of the QSRCAC algorithm is presented in this section. Subsection 3.1 presents a brief review of RCAC. Subsection 3.2 describes an online gradient estimator based on the Kalman filter. Subsection 3.3 expands RCAC presented in Subsection 3.1 to include gradient estimates obtained via the technique presented in Subsection 3.2, resulting in QSRCAC.

Review of retrospective cost adaptive control

RCAC is described in detail in Rahman, Xie, and Bernstein (2017). In this subsection we summarize the main elements of this method. Consider the strictly proper, discrete-time, input-output controller

$$u_k = \sum_{i=1}^{l_c} P_{i,k} u_{c,k-i} + \sum_{i=1}^{l_c} Q_{i,k} z_{k-i}, \tag{1}$$

where $k \geq 0$ is the time step, $u_k \in \mathbb{R}^{l_u}$ is the controller output and thus the control input, $u_{c,k} \in \mathbb{R}^{l_u}$ is the constrained control input, $z_k \in \mathbb{R}^{l_z}$ is the measured performance variable, l_c is the controller-window length, and, for all $i \in \{1, \ldots, l_c\}$, $P_{i,k} \in \mathbb{R}^{l_u \times l_u}$ and $Q_{i,k} \in \mathbb{R}^{l_u \times l_z}$ are the controller coefficient matrices. In particular, $u_{c,k}$ results from applying system constraints to u_k, as defined in (35) in Subsection 5.2. The controller shown in (1) can be written as

$$u_k = \phi_k \theta_k, \tag{2}$$

where

$$\phi_k \triangleq \begin{bmatrix} u_{\mathrm{c},k-1}^T & \cdots & u_{\mathrm{c},k-l_{\mathrm{c}}}^T & z_{k-1}^T & \cdots & z_{k-l_{\mathrm{c}}}^T \end{bmatrix} \otimes I_{l_{\mathrm{u}}} \in \mathbb{R}^{l_{\mathrm{u}} \times l_\theta}, \tag{3}$$

$$\theta_k \triangleq \mathrm{vec}\begin{bmatrix} P_{1,k} & \cdots & P_{l_{\mathrm{c}},k} & Q_{1,k} & \cdots & Q_{l_{\mathrm{c}},k} \end{bmatrix} \in \mathbb{R}^{l_\theta}, \tag{4}$$

$l_\theta \triangleq l_{\mathrm{c}} l_{\mathrm{u}} (l_{\mathrm{u}} + l_{\mathrm{z}})$, θ_k is the vector of controller coefficients, which are updated at each time step k, and $\otimes$ is the Kronecker product.

Next, define the retrospective cost variable

$$\hat{z}_k(\hat{\theta}) \triangleq z_k - G_{\mathrm{f}}(\mathbf{q})(u_k - \phi_k \hat{\theta}), \tag{5}$$

where $\hat{z}_k$ is the retrospective-cost variable, G_{f} is an $l_{\mathrm{z}} \times l_{\mathrm{u}}$ asymptotically stable, strictly proper transfer function, $\mathbf{q}$ is the forward-shift operator, and $\hat{\theta} \in \mathbb{R}^{l_\theta}$ is the controller coefficient vector determined by optimization below. The rationale underlying (5) is to replace the applied past control inputs with the re-optimized control input $\phi_k \hat{\theta}$, as mentioned in Rahman, Xie, and Bernstein (2017) and Islam et al. (2021).

In the present work, G_{f} is chosen to be a finite-impulse-response transfer function of window length l_{f} of the form

$$G_{\mathrm{f}}(\mathbf{q}) \triangleq \sum_{i=1}^{l_{\mathrm{f}}} N_{i,k} \mathbf{q}^{-i}, \tag{6}$$

where $N_{1,k}, \ldots, N_{l_{\mathrm{f}},k} \in \mathbb{R}^{l_{\mathrm{z}} \times l_{\mathrm{u}}}$. We can thus rewrite (5) as

$$\hat{z}_k(\hat{\theta}) = z_k - N_k(U_{\mathrm{c},k} - \Phi_k \hat{\theta}), \tag{7}$$

where

$$\Phi_k \triangleq \begin{bmatrix} \phi_{k-1} \\ \vdots \\ \phi_{k-l_{\mathrm{f}}} \end{bmatrix} \in \mathbb{R}^{l_{\mathrm{f}} l_{\mathrm{u}} \times l_\theta}, \quad U_{\mathrm{c},k} \triangleq \begin{bmatrix} u_{\mathrm{c},k-1} \\ \vdots \\ u_{\mathrm{c},k-l_{\mathrm{f}}} \end{bmatrix} \in \mathbb{R}^{l_{\mathrm{f}} l_{\mathrm{u}}}, \tag{8}$$

$$N_k \triangleq \begin{bmatrix} N_{1,k} \cdots N_{l_{\mathrm{f}},k} \end{bmatrix} \in \mathbb{R}^{l_{\mathrm{z}} \times l_{\mathrm{f}} l_{\mathrm{u}}}. \tag{9}$$

In most applications, the filter coefficient matrix N_k is constant and is determined by features of the system being controlled, as mentioned in Rahman, Xie, and Bernstein (2017). Other applications may require N_k to be constructed and updated online using data, as mentioned in Islam et al. (2021). For the present work, N_k is updated online and is used to determine a direction based on the estimated gradient of the performance variable z_k. The algorithm used to determine N_k at each step k is given in the next section.

Using (5), we define the cumulative cost function

$$J_{\mathrm{R},k}(\hat{\theta}) \triangleq \sum_{i=0}^{k} [\hat{z}_i^{\mathrm{T}}(\hat{\theta}) \hat{z}_i(\hat{\theta}) + (\phi_i \hat{\theta})^{\mathrm{T}} R_{\mathrm{u}} \phi_i \hat{\theta}] + (\hat{\theta} - \theta_0)^{\mathrm{T}} P_0^{-1} (\hat{\theta} - \theta_0), \tag{10}$$

where $P_0 \in \mathbb{R}^{l_\theta \times l_\theta}$ is positive definite and $R_u \in \mathbb{R}^{l_u \times l_u}$ is positive semidefinite. The following result uses recursive least squares (RLS), as mentioned in Ljung and Soderstrom (1983) and Islam and Bernstein (2019), to minimize (10), where, at each step k, the minimizer of (10) provides the update θ_{k+1} of the controller coefficient vector θ_k.

Proposition. Let P_0 be positive definite, and R_u be positive semidefinite. Then, for all $k \geq 0$, unique global minimizer θ_k of (10) is given by

$$P_k = P_{k-1} - P_{k-1} \begin{bmatrix} N_{k-1}\Phi_{k-1} \\ \phi_{k-1} \end{bmatrix}^T \Gamma_{k-1} \begin{bmatrix} N_{k-1}\Phi_{k-1} \\ \phi_{k-1} \end{bmatrix} P_{k-1}, \tag{11}$$

$$\theta_k = \theta_{k-1} - P_k \begin{bmatrix} N_{k-1}\Phi_{k-1} \\ \phi_{k-1} \end{bmatrix}^T \bar{R} \begin{bmatrix} z_{k-1} - N_{k-1}(U_{c,k-1} - \Phi_{k-1}\theta_{k-1}) \\ \phi_{k-1}\theta_{k-1} \end{bmatrix}, \tag{12}$$

where

$$\Gamma_{k-1} \triangleq \bar{R} - \bar{R} \begin{bmatrix} N_{k-1}\Phi_{k-1} \\ \phi_{k-1} \end{bmatrix} \left(P_{k-1}^{-1} + \begin{bmatrix} N_{k-1}\Phi_{k-1} \\ \phi_{k-1} \end{bmatrix}^T \bar{R} \begin{bmatrix} N_{k-1}\Phi_{k-1} \\ \phi_{k-1} \end{bmatrix} \right)^{-1} \begin{bmatrix} N_{k-1}\Phi_{k-1} \\ \phi_{k-1} \end{bmatrix}^T \bar{R}$$

$$\in \mathbb{R}^{(l_z+l_u)\times(l_z+l_u)}, \tag{13}$$

$$\bar{R} \triangleq \mathrm{diag}(I_{l_z}, R_u) \in \mathbb{R}^{(l_z+l_u)\times(l_z+l_u)}. \tag{14}$$

For all of the numerical simulations and physical experiments in this work, θ_k is initialized as $\theta_0 = 0$ to reflect the absence of additional prior modeling information. The matrices P_0 and R_u have the form $P_0 = p_0 I_{l_\theta}$ and $R_u = r_u I_{l_u}$, where the positive scalar p_0 and nonnegative scalar r_u determine the rate of adaptation. Hence, the hyperparameters required by RCAC are l_c, p_0, and r_u.

Online gradient estimator using a Kalman filter

For all $k \geq 0$, let $J_k \triangleq [J_{1,k} \cdots J_{l_J,k}]^T \in \mathbb{R}^{l_J}$ be a cost function vector computed from system measurements, where, for all $i \in \{1, \ldots, l_J\}$, $J_{i,k} \geq 0$ is the ith component of J_k, let $u_{c,k}$ be the constrained control input defined in (35) in Subsection 5.2, and let $\mathscr{J}_k \triangleq [\mathscr{J}_{1,k} \cdots \mathscr{J}_{l_J,k}]^T \in \mathbb{R}^{l_J \times l_u}$ be the gradient of J_k over $u_{c,k}$, where, for all $i \in \{1, \ldots, l_J\}$, the transpose of $\mathscr{J}_{i,k} \in \mathbb{R}^{l_u}$ corresponds to the ith row of $\mathscr{J}_k$.

Next, let $i \in \{1, \ldots, l_J\}$. Consider the measurement model for $J_{i,k}$

$$J_{i,k} = J_{b,i} + \mathscr{J}_{i,k}^T u_{c,k}, \tag{15}$$

where $J_{b,i} \in \mathbb{R}$ is a bias variable. Note that (15) is an extension of (17) from Gelbert et al. (2012). Furthermore, let $\hat{\mathscr{J}}_{i,k} \in \mathbb{R}^{l_u}$ be an estimate of $\mathscr{J}_{i,k}$, let $\hat{J}_{b,i} \in \mathbb{R}$ be an estimate of $J_{b,i}$, let $\hat{x}_{i,k} \triangleq [\hat{\mathscr{J}}_{i,k}^T \quad \hat{J}_{b,i}]^T \in \mathbb{R}^{l_u+1}$ be an estimate of $x_{i,k} \triangleq [\mathscr{J}_{i,k}^T \quad J_{b,i}]^T$, and let

$P_{i,k} \in \mathbb{R}^{(l_\mathrm{u}+1) \times (l_\mathrm{u}+1)}$ be the covariance of the estimate $\hat{x}_{i,k}$ of $x_{i,k}$. Then, as indicated by (15) and Section 3.1 of Gelbert et al. (2012), the estimate $\hat{J}_{i,k}$ can be obtained using a Kalman filter (KF) with state and measurement equations given by

$$x_{i,k+1} = x_{i,k} + w_{i,k}, \tag{16}$$

$$y_{i,k} \overset{\Delta}{=} \begin{bmatrix} J_{i,k} \\ J_{i,k-k_1} \\ \vdots \\ J_{i,k-k_{l_\mathrm{u}}} \end{bmatrix} = \begin{bmatrix} u_{\mathrm{c},k-1}^T & 1 \\ u_{\mathrm{c},k-1-k_1}^T & 1 \\ \vdots & \vdots \\ u_{\mathrm{c},k-1-k_{l_\mathrm{u}}}^T & 1 \end{bmatrix} x_{i,k} + v_{i,k}, \tag{17}$$

where $y_{i,k} \in \mathbb{R}^{l_\mathrm{u}+1}$ is the measurement vector $w_{i,k}, v_{i,k} \in \mathbb{R}^{l_\mathrm{u}+1}$ are Gaussian random variables, and $0 < k_1 < \ldots < k_{l_\mathrm{u}}$ are user-chosen indices. Note that l_u indices are needed to ensure that $x_{i,k}$ is observable, as stated in Section 2.2 of Gelbert et al. (2012). Furthermore, in Section 2.2 of Gelbert et al. (2012), indices $k_1, \ldots, k_{l_\mathrm{u}}$ are chosen based on the period of a perturbation signal added to the input to ensure good conditioning of the observability Gramian corresponding to (16), (17) and thus enhance the accuracy of the estimate $\hat{x}_{i,k}$; a similar rationale is used in this paper to choose these indices based on the perturbation signal introduced in Subsection 3.3.

Hence, it follows from (16), (17) that the estimate $\hat{J}_{i,k}$ is given by the recursive update of the KF, whose prediction and update equations are given, for $i \in \{1, \ldots, l_\mathrm{J}\}$, by

$$\hat{x}_{i,k} = \hat{x}_{i,k-1} + K_{i,k-1}\big(G_{i,k-1} - H_{k-1}\hat{x}_{i,k-1}\big), \tag{18}$$

$$P_{i,k} = (I_{l_\mathrm{u}+1} - K_{i,k-1}H_{k-1})(P_{i,k-1} + Q_i), \tag{19}$$

$$\hat{J}_{i,k} = [I_{l_\mathrm{u}} \quad 0_{l_\mathrm{u} \times 1}]\hat{x}_{i,k}, \tag{20}$$

where

$$G_{i,k-1} \overset{\Delta}{=} \begin{bmatrix} J_{i,k-1} \\ J_{i,k-1-k_1} \\ \vdots \\ J_{i,k-1-k_{l_\mathrm{u}}} \end{bmatrix} \in \mathbb{R}^{l_\mathrm{u}+1}, H_{k-1} \overset{\Delta}{=} \begin{bmatrix} u_{\mathrm{c},k-1}^T & 1 \\ u_{\mathrm{c},k-1-k_1}^T & 1 \\ \vdots & \vdots \\ u_{\mathrm{c},k-1-k_{l_\mathrm{u}}}^T & 1 \end{bmatrix} \in \mathbb{R}^{(l_\mathrm{u}+1) \times (l_\mathrm{u}+1)},$$

$$K_{i,k-1} \overset{\Delta}{=} [(P_{i,k-1} + Q_i)H_{k-1}^T][H_{k-1}(P_{i,k-1} + Q_i)H_{k-1}^T + R_i]^{-1} \in \mathbb{R}^{(l_\mathrm{u}+1) \times (l_\mathrm{u}+1)},$$

and $Q_i, R_i \in \mathbb{R}^{(l_\mathrm{u}+1) \times (l_\mathrm{u}+1)}$ are user-chosen constant weighting matrices. The matrices Q_i and R_i determine the rate of estimation and the susceptibility of the estimate $\hat{x}_{i,k}$ to measurement noise. Finally, the estimate $\hat{J}_k$ is given by

$$\hat{J}_k \overset{\Delta}{=} \begin{bmatrix} \hat{J}_{1,k} \cdots & \hat{J}_{l_\mathrm{J},k} \end{bmatrix}^T \in \mathbb{R}^{l_\mathrm{J} \times l_\mathrm{u}}. \tag{21}$$

For all of the numerical simulations and laboratory experiments in the present work, $\hat{x}_{i,k}$ is initialized as $\hat{x}_{i,0} = 0$. The matrices $P_{i,0}$, Q_i, and R_i have the form $P_{i,0} = p_{i,0}I_{l_u+1}$, $Q_i = q_iI_{l_u+1}$, and $R_i = r_iI_{l_u+1}$, where the positive scalars $p_{i,0}, q_i$, and r_i determine the rate of estimation. Hence, the hyperparameters required by the KF are $p_{i,0}, q_i$, and r_i, for all $i \in \{1, \ldots, l_J\}$, and k_j for all $j \in \{1, \ldots, l_u\}$.

Quasi-static RCAC

As shown in Figure 3, QSRCAC includes RCAC described in Subsection 3.1, the KF gradient estimator described in Subsection 3.2, a normalization function, and a gradient conversion function. For QSRCAC, $l_J = l_z$ and $l_f = l_u$. QSRCAC operates on the previous time step cost-function vector $J_{k-1} \in \mathbb{R}^{l_z}$ and $u_{c,k-1} \in \mathbb{R}^{l_u}$ to produce the output vector $\tilde{u}_k \in \mathbb{R}^{l_u}$. As mentioned in subsection 3.2, for all $i \in \{1, \ldots, l_z\}$, $J_{i,k-1} > 0$. The objective of QSRCAC is to minimize the components of J_k by modulating $\tilde{u}_k$, that is,

$$\min_{(\tilde{u}_n)_{n=0}^{\infty}} \limsup_{k \to \infty} \sum_{i=1}^{l_z} J_{i,k}. \tag{22}$$

The performance variable z_{k-1} used by RCAC is obtained by normalizing J_{k-1} using

$$z_{k-1} \triangleq [I_{l_z} + \nu \operatorname{diag}(J_{k-1})]^{-1}J_{k-1}, \tag{23}$$

where $\nu \in [0, \infty)$. We fix $\nu = 0.2$ throughout the present work. Next, the gradient estimator block operates on J_{k-1} and u_{k-1} to produce $\hat{J}_k$ by using the KF-based estimator described in Subsection 3.2. The gradient conversion block yields $N_{k-1} = [N_{1,k-1} \quad \cdots \quad N_{l_u,k-1}]$, such that, for all $i \in \{1, \ldots, l_u\}$,

$$N_{i,k-1} = \begin{bmatrix} & \overline{\hat{J}}_{1,i,k} & \\ 0_{l_z \times (i-1)} & \vdots & 0_{l_z \times (l_u-i)} \\ & \underline{\hat{J}}_{l_z,i,k} & \end{bmatrix}, \tag{24}$$

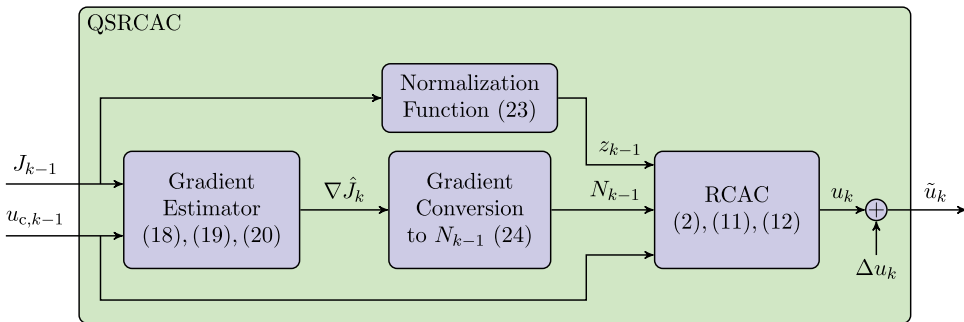where, for all $j \in \{1, \ldots, l_z\}$,

Figure 3. QSRCAC block diagram.

$$\bar{\hat{J}}_{j,i,k} \triangleq \begin{cases} \hat{\bar{J}}_{j,i,k}/\parallel \hat{\bar{J}}_{j,k} \parallel, & \parallel \hat{\bar{J}}_{j,k} \parallel \geq \varepsilon \\ \bar{\hat{J}}_{j,i,k-1}/\varepsilon, & otherwise, \end{cases} \tag{25}$$

$\hat{\bar{J}}_{j,i,k}$ is the ith component of $\hat{\bar{J}}_{j,k}$, and $\varepsilon > 0$. Note that N_k converges in the case where $\lim_{k\to\infty} \hat{\bar{J}}_k = 0$, and thus N_k converges when QSRCAC converges to an operating point. We fix $\varepsilon = 10^{-4}$ throughout the present work. The RCAC block then uses z_{k-1}, N_{k-1}, and u_{k-1} to produce $u_k \in \mathbb{R}^{l_u}$ by using the operations described in Subsection 3.1.

Finally, define $\tilde{u}_k \triangleq u_k + \Delta u_k$, where $\Delta u_k \in \mathbb{R}^{l_u}$ is a perturbation signal, which is defined in Subsection 5.2. Note that $u_{c,k-1}$ is shown as an input to QSRCAC since the output $\tilde{u}_k$ may be subject to constraints. Hence, $u_{,k-1}$ is obtained from $\tilde{u}_k$ after constraints and a 1-step delay is applied. Note that, while Gelbert et al. (2012) uses only $\hat{\bar{J}}_k$, QSRCAC uses J_{k-1} and $\hat{\bar{J}}_k$.

In numerical simulations and laboratory experiments, the KF and RCAC are enabled and disabled in various ways. We consider the following modes of operation of QSRCAC starting at step $k_0 \geq 0$:

i) *Mode 1: KF and RCAC are disabled.* For all $k \geq k_0$, $\theta_k = \theta_{k-1}$, $P_k = P_{k-1}$, $u_k = 0$, $\Delta u_k = 0$, and, for all $i \in \{1, \ldots, l_z\}$, $\hat{x}_{i,k} = \hat{x}_{i,k-1}$, $P_{i,k} = P_{i,k-1}$, and $\hat{\bar{J}}_{i,k} = 0$.

ii) *Mode 2: KF is enabled and RCAC is disabled.* For all $k \geq k_0$, $\theta_k = \theta_{k-1}$, $P_k = P_{k-1}$, $u_k = 0$, $\Delta u_k = \mathcal{H}(k)$, where $\mathcal{H} : \{0, 1, \ldots\} \to \mathbb{R}^{l_u}$ is a nonzero, periodic vector function, and, for all $i \in \{1, \ldots, l_z\}$, $\hat{x}_{i,k}$, $P_{i,k}$, and $\hat{\bar{J}}_{i,k}$, are updated by (18), (19) and (20), respectively.

iii) *Mode 3: KF and RCAC are enabled.* For all $k \geq k_0$, θ_k, P_k, and u_k are updated by (11), (12), and (2), respectively, $\Delta u_k = 0$, and, for all $i \in \{1, \ldots, l_z\}$, $\hat{x}_{i,k}$, $P_{i,k}$, and $\hat{\bar{J}}_{i,k}$, are updated by (18), (19) and (20), respectively.

Note that Δu_k is nonzero only in Mode 2, unlike in Gelbert et al. (2012), where the perturbation signal is never zero over any period of time. Hence, Δu_k is used only to initialize the KF and it does not affect the adaptation of RCAC. Furthermore, the rationale for choosing $k_1, \ldots, k_{l_u}$ mentioned in Subsection 3.2 is based on $\mathcal{H}$. For the current application, $\mathcal{H}$ and the values of $k_1, \ldots, k_{l_u}$ are given in Subsection 5.2.

Control objectives and experimental operating conditions

The combustion dynamics presented Section 2 typically have timescales of less than 3 ms. In contrast, the response of the mass flow control system to a change in commanded mass flow rate is relatively slow due to the slow response of the electronic pressure controller and the inertia of the fluid delivery systems, although the sensor update rate of the pressure controllers is 25 ms. As an example, the rise time of the mass flow rate in the air feed lines to a step command change of 0.5 g/s is 0.2 s as shown in Figure 4. Hence, the present work implements QSRCAC, a quasi-static adaptive control technique that operates with actuators that have low bandwidth relative to the dynamics of the combustor.

For the QSRCAC tests in the present work, the mass flow rates through the secondary air feeds are maintained at zero, that is, the variation of swirl numbers is not considered in the present work, and $\dot{m}_f$ is kept constant after the initial conditions are reached by the MCS. Hence, only $\dot{m}_i$ and $\dot{m}_o$ are modulated by QSRCAC in the present work. Note that this
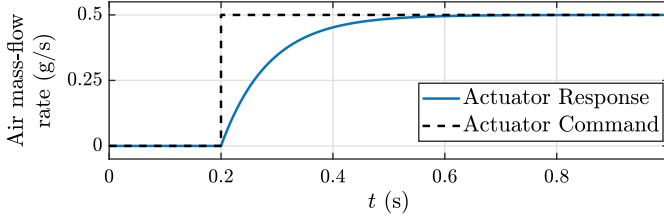
Figure 4. Air mass flow rate response of the DISCo pressure regulator to a step command of 0.5 g/s.

arrangement simplifies the control problem by diminishing the amount of modulated system inputs and allows for the indirect modulation of ϕ and R.

The control objectives considered in the present work are discussed next. Let $p' \in \mathbb{R}$ be the measured pressure fluctuations in kPa, $p'_{rms} > 0$ be the RMS of p', $l_{rms} > 0$ be the number of samples used to compute the RMS, and let $\tau_{rms} > 0$ be the RMS sampling period such that, for all $t \geq l_{rms}\tau_{rms}$,

$$p'_{rms}(t) \overset{\Delta}{=} \sqrt{\frac{1}{l_{rms}} \sum_{\kappa=0}^{l_{rms}} [p'(t - \kappa\, \tau_{rms})]^2}. \tag{26}$$

Let $T \in \mathbb{R}$ be the temperature measured at the exit of the combustor in K, and let $T_{ref} \in \mathbb{R}$ be the commanded/reference combustor exit temperature in K. As mentioned in Section 1, the control objectives of the current work include the mitigation of thermoacoustic oscillations and reaching a user-defined temperature. Hence, two types of tests of increasing complexity are performed in the present work to address these control objectives:

- *Two-input, single-output (TISO) test*: The controller yields inner swirler and outer swirler air mass flow rates, $\dot{m}_i$ and $\dot{m}_o$ respectively (two system inputs), to reduce p'_{rms} (one measured output).
- *Two-input, two-output (TITO) test*: The controller yields inner swirler and outer swirler air mass flow rates, $\dot{m}_i$ and $\dot{m}_o$ respectively (two system inputs), to reduce p'_{rms} and reach T_{ref}, such that $(T - T_{ref})^2$ is reduced (two measured outputs).

The single-objective TISO test is used to assess the effectiveness of QSRCAC in reducing the amplitude of thermoacoustic instabilities in DISCo. The multi-objective TITO test presents a problem of more practical relevance in a power generation unit, that is, reducing the amplitude of thermoacoustic instabilities while commanding a change in the combustor exit temperature, mimicking a net power variation. It is important to note that no information on the flame position and structure of the flame is provided to the controller to satisfy the temperature goal. As will be seen later in Section 6.3, this has major implications on the results. In both tests, the pressure fluctuation measurements from the pressure sensor in the combustor chamber are used to compute p'_{rms}. In the TITO test, the averaged temperature obtained from the three thermocouples (shown in Figure 1) at the combustor exit is subtracted from the commanded combustor exit temperature to determine the command-following error.

Table 1. Range of operating conditions of DISCo considered in this study.

Parameter	Values or range
Fuel mass flow rate $\dot{m}_f$ (g/s)	{0.372, 0.396, 0.419}
Air mass flow rate per swirler $\dot{m}_i, \dot{m}_o$ (g/s)	[0.75, 9]
Equivalence ratio ϕ	[0.6, 1]

Table 1 shows the operating conditions of DISCo used for both tests. Three different values of $\dot{m}_f$ are used in the TISO and TITO tests. The $\dot{m}_i$ and $\dot{m}_o$ ranges are derived from actuator constraints and the ϕ range is chosen to prevent flameout. As mentioned in Section 1, to allow the controller to focus on these objectives, low ϕ values near the lean blowout limit are not sought in the present work. Since $\dot{m}_f$ is kept constant throughout the QSRCAC experiments, the operating ranges of $\dot{m}_i, \dot{m}_o$, and ϕ impose a convex constraint on $\dot{m}_i$ and $\dot{m}_o$, which is addressed in Subsection 5.2.

Numerical simulations for hyperparameter selection

A crucial aspect of QSRCAC is the selection of hyperparameters, which determine the rate of adaptation, the controller order, and the controller performance. QSRCAC requires 3 + 3 $l_z + l_u$ hyperparameters corresponding to RCAC and KF, as mentioned at the end of Subsections 3.1 and 3.2, respectively. Furthermore, the cost function used by QSRCAC also requires hyperparameters, as described in Subsection. 5.2. The hyperparameter selection methodology used in the present work is based on numerical simulations, as shown in Figure 5; this methodology was also used in Paredes, Islam, and Bernstein (2022); Paredes and Bernstein (2023).

First, laboratory experiments are conducted in an open-loop configuration (no feedback control) to obtain pressure fluctuation and temperature measurements from DISCo at operating points chosen using a DoE based approach. Then, a fit procedure is applied to the pressure and temperature measurements obtained at these operating points to generate a simulation model of DISCo. This simulation model is then used in closed-loop (with feedback control) numerical simulations to select the hyperparameters of QSRCAC based on how well the control objectives described in Section 4 are met. The selected hyperparameters are then used in subsequent physical closed-loop DISCo laboratory experiments in Section 6. Note that the simulation model is used only to select hyperparameters for the controller, but is otherwise not used or needed for feedback control.

The fit procedure and the DISCo model are described in Subsection 5.1, the sampled data implementation and configuration of QSRCAC with the DISCo simulation model is described in Subsection 5.2, and the results of the closed-loop numerical simulations are
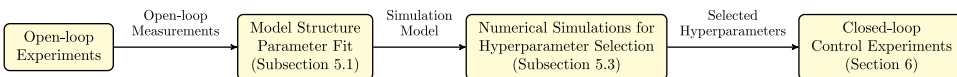

Figure 5. Hyperparameter selection methodology. The objective is to select hyperparameters by applying the quasi-static adaptive controller to a low-accuracy simulation model of DISCo. The selected hyperparameters are then used in physical closed-loop experiments.

shown in Subsection 5.3. The values of the chosen hyperparameters are summarized in Table 4.

DISCo simulation model

The motivation for the development of a DISCo simulation model with a low resource cost is explained next. Extended steady state operation of a combustor is challenging for multiple reasons, primarily due to the large amount of heat generated during combustion. For instance, exposing components such as sensors and seals to high temperatures for long periods of time diminishes their lifespan. However, control algorithms can have a large number of hyperparameters that need to be carefully selected to achieve the best performance. This would involve running several closed-loop tests in the combustor while iterating through several combinations of hyperparameters. This can be both time consuming and resource intensive. For this reason, a mathematical representation of the combustor response to a given set of input variables is developed in this section. This empirical model captures variations in pressure fluctuations that arises due to changes in the combustor input variables described next. Influences of factors such as combustor geometry and the turbulent combustion process are not explicitly modeled. The resulting DISCo simulation model can be run several times in a computer without incurring in high resource costs.

The simulation model is a multi-dimensional curve fit of the response (output) of the combustor as a function of design variables (inputs) is constructed using the response surface methodology (RSM) approach (DeLoach 2000). For the curve fit in the present work, the considered input variables are $\dot{m}_t \in [6,\ 12]$ g/s, $\phi \in [0.6,\ 1]$, and $R \in [0.1,\ 10]$, and the response variable is p'_{rms}. A model for the combustor exit temperature is considered later in this section. The procedure involves dividing the input variables into evenly spaced regions in the sample space and choosing a controlled random sample using Latin hypercube sampling (LHS). The main advantages of LHS is that it produces samples that reflect the true underlying distribution and that it tends to require much smaller sample sizes than simple random sampling, which is particularly advantageous in high dimensional problems. A total of 170 open-loop experiments are conducted on the combustor and p'_{rms} is calculated at each point using (26) with $\tau_{\mathrm{rms}} = 6.25 \cdot 10^{-5}$ s and $l_{\mathrm{rms}} = 1/\tau_s$ to use about 1 s of data with a sampling frequency of 16 kHz. A response surface is constructed using the Minitab software considering linear, square and two-way interaction terms. The generated surface has a R^2 of 69% and is given in terms of $\dot{m}_f, \dot{m}_i$, and $\dot{m}_o$ by

$$
\begin{aligned}
p'_{\mathrm{rms}}(\dot{m}_f, \dot{m}_i, \dot{m}_o) = &-0.132\dot{m}_i^2 + 0.269\dot{m}_o^2 + 0.361\dot{m}_i\dot{m}_o - 3.719\dot{m}_o\dot{m}_f - 0.278\dot{m}_i \\
&- 2.262\dot{m}_o + 35.6\dot{m}_f - 0.08.
\end{aligned}
\tag{27}
$$

The dimension of (27) can be reduced by assigning $\dot{m}_f$ a constant value, which allows the model to better emulate the closed-loop experiments, in which only $\dot{m}_i$ and $\dot{m}_o$ are modulated by QSRCAC. While the simulation model represented by (27) is not high-fidelity, it is sufficiently accurate for the hyperparameter selection procedure, as is shown by the experimental results in Subsection 6.2.

An overview of the dynamics of the DISCo simulation model is given next. Let $\dot{m}_{sp}(t) \triangleq \left[\dot{m}_{sp,i}(t)\dot{m}_{sp,o}(t)\right]^T \in \mathbb{R}^2$ be the specified air mass flow rate vector and the model input, where $\dot{m}_{sp,i}, \dot{m}_{sp,o} \in \mathbb{R}$ are the specified inner and outer swirl air mass flow rates, respectively. The dynamics of the pressure regulators are thus modeled by

$$\ddot{m}(t) = -a\dot{m}(t) + b\dot{m}_{sp}(t), \tag{28}$$

where $\dot{m}(t) \triangleq \left[\dot{m}_i(t)\dot{m}_o(t)\right]^T \in \mathbb{R}^2$ is the air mass flow rate vector, and $a, b > 0$. Next, let $\mathcal{F}, \mathcal{G} : \mathbb{R}^2 \to \mathbb{R}$ be the static maps defined as

$$\mathcal{F}(\dot{m}) \triangleq -0.132\dot{m}_i^2 + 0.269\dot{m}_o^2 + 0.361 \cdot 10^{-2}\dot{m}_i\dot{m}_o - 0.278\dot{m}_i - 3.7496\dot{m}_o + 14.16, \tag{29}$$

$$\mathcal{G}(\dot{m}) \triangleq \frac{1}{32}(\dot{m}_i - \dot{m}_o)^2 - \frac{1}{32}\left[\dot{m}_i + \dot{m}_o - (\dot{m}_{min} + \dot{m}_{max})\right]^2 + 3, \tag{30}$$

where $\dot{m}_{min}, \dot{m}_{max} > 0$ are the minimum and maximum air mass flow rates allowed per swirler, respectively. The function $\mathcal{F}$ is obtained by setting $\dot{m}$ to a constant value in (27). In particular, $\dot{m}_f \equiv 0.4$ g/s for all simulation tests, which is close to the value of 0.396 g/s shown in Table 1. Note that the output values of $\mathcal{F}$ are similar to the RMS of the voltage measurements obtained from the pressure sensors. An approximate structure of $\mathcal{G}$ is chosen by leveraging knowledge from the combustor response. At the maximum and minimum values of R, higher combustor exit temperatures are expected due to an elongated and distributed region of heat release. The coefficients of $\mathcal{G}$ are chosen to fit the voltage measurements obtained from the temperature sensors and rounded to integer values. The output values of $\mathcal{F}$ and $\mathcal{G}$ for all $\dot{m}_i, \dot{m}_o \in [1, 9]$ g/s are shown in Figure 6.

Next, we define the model output $y(t) \triangleq \left[\hat{p}'(t) \ \hat{T}(t)\right]^T$, where $\hat{p}'(t) \in \mathbb{R}$ is the normalized pressure fluctuation and $\hat{T}(t) > 0$ is the normalized combustor exit temperature. The values of $\hat{p}'(t)$ and $\hat{T}(t)$ are normalized such that they follow the voltage measurements
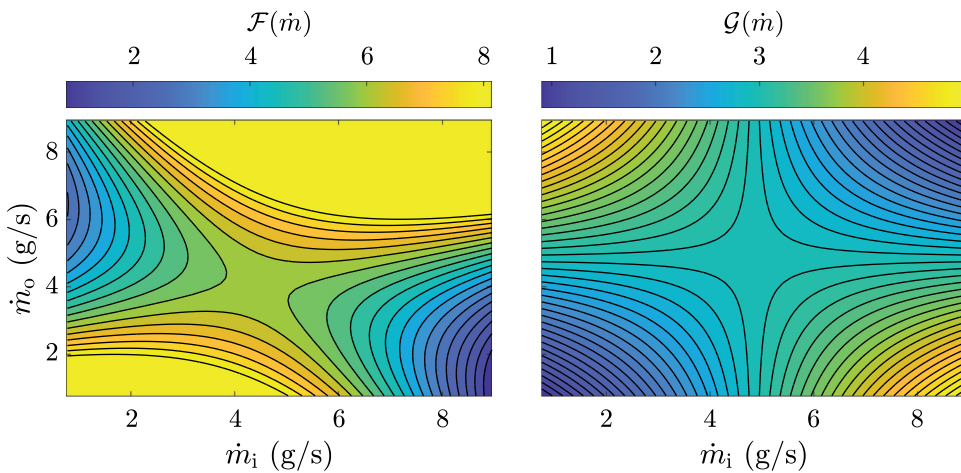

Figure 6. $\mathcal{F}(\dot{m})$ and $\mathcal{G}(\dot{m})$ output values, where $\dot{m} = [\dot{m}_i \ \dot{m}_o]^T \in [1, 9] \times [1, 9]$ g/s. For visualization, the values corresponding to $\mathcal{F}(\dot{m}) > 8.2$ are saturated at 8.2.

obtained from the pressure and temperature sensors in open-loop experiments. Then, $\hat{p}'(t)$ and $\hat{T}(t)$ are given by

$$\hat{p}'(t) = \mathcal{F}(\dot{m}(t))\sin(2\pi f_0 t) + w_1(t), \tag{31}$$

$$\hat{T}(t) = \mathcal{G}(\dot{m}(t)) + w_2(t), \tag{32}$$

where $f_0 > 0$, and $w_1(t)$ and $w_2(t)$ are noise signals. In particular, for all $k \geq 0$ and all $t \in [k\tau_{\text{sim}}, (k+1)\tau_{\text{sim}})$, where $\tau_{\text{sim}} > 0$ is the simulation time step, $w_1(t)$ and $w_2(t)$ are given by $w_1(t) = \omega_{1,k}$ and $w_2(t) = \omega_{2,k}$, where $\omega_{1,k}$ is a Gaussian random variable with mean 0 and standard deviation σ_1, and $\omega_{2,k}$ is a Gaussian random variable with mean 0 and standard deviation σ_2.

The block diagram in Figure 7 summarizes these dynamics. Table 2 shows the DISCo simulation model parameters, where a and b are chosen to match the response of the pressure regulators, the frequency f_0 corresponds to a value close to the second highest peak shown in Figure 2b, σ_1 and σ_2 are chosen to match the signal-to-noise ratio of the pressure-fluctuation and temperature measurements, and $\tau_{\text{sim}} = 10^{-4}$ s corresponds to the sampling rate of the sensors.

Sampled-data implementation and configuration of QSRCAC for DISCo numerical simulations

QSRCAC is implemented as a sampled-data controller to control the response of the DISCo simulation model described in Subsection 5.1. Since both the inner and outer swirl mass flow rates are modulated, it follows that $l_u = 2$. As mentioned in Section 4, the value of l_z depends on the test being performed; in particular, $l_z = 1$ for the TISO tests and $l_z = 2$ for the TITO tests. Figure 8 shows the block diagram of the sampled-data closed-loop system considered for numerical simulations, where $\overline{u} \in \mathbb{R}^2$ is the command bias, $\tau_{\text{rms}} > 0$ is the
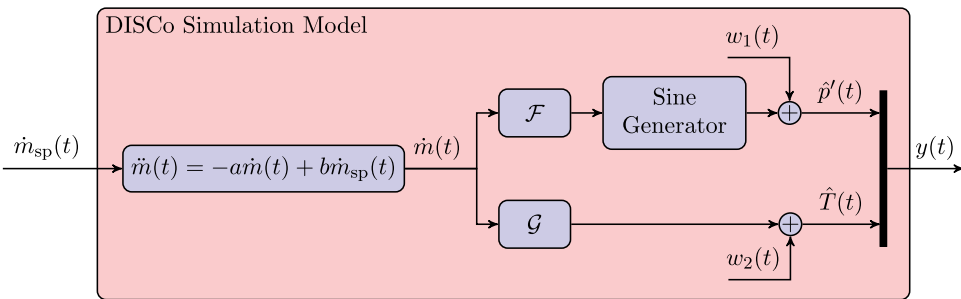

Figure 7. DISCO simulation model block diagram.

Table 2. Parameters of the DISCo simulation model.

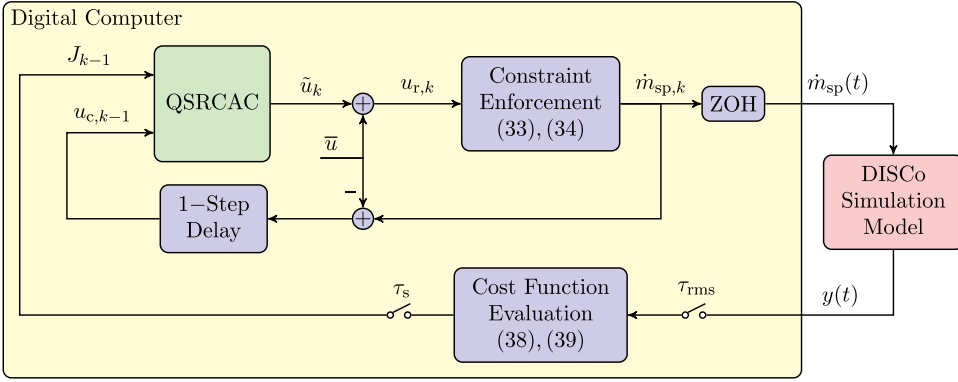| Parameter	a	b	f_0	σ_1	σ_2	τ_{sim}
Unit	-	-	Hz	-	-	s
Value	110	110	500	0.1	0.05	10^{-4}

Figure 8. Sampled-data implementation of QSRCAC for DISCo simulation.

RMS sampling period given by $\tau_{\mathrm{rms}} = \tau_{\mathrm{sim}} = 10^{-4}$ s/step, and $\tau_{\mathrm{s}} > 0$ is the adaptive controller sampling period given by $\tau_{\mathrm{s}} = 2000\,\tau_{\mathrm{sim}} = 2000\,\tau_{\mathrm{rms}} = 0.2$ s/step. The command bias $\overline{u}$ encodes the initial $\dot{m}_{\mathrm{i}}$ and $\dot{m}_{\mathrm{o}}$ operating point set by the MCS. The D/A and A/D interfaces, which are synchronous, are a zero-order-hold (ZOH) and instantaneous sampler, respectively.

Let the requested command $u_{\mathrm{r},k}$ be given by $u_{\mathrm{r},k} \overset{\Delta}{=} \tilde{u}_k + \overline{u}$. Then, the constraints discussed in Section 4 are applied to $u_{\mathrm{r},k}$ to obtain $\dot{m}_{\mathrm{sp},k}$, which is given by

$$\dot{m}_{\mathrm{sp},k} \overset{\Delta}{=} \begin{bmatrix} \dot{m}_{\mathrm{sp,i},k} & \dot{m}_{\mathrm{sp,o},k} \end{bmatrix}^T \overset{\Delta}{=} \underset{v \overset{\Delta}{=} \begin{bmatrix} v_{\mathrm{i}} & v_{\mathrm{o}} \end{bmatrix}^T \in \mathbb{R}^2}{\arg\min} \, ||u_{\mathrm{r},k} - v||_2, \tag{33}$$

subject to

$$\begin{aligned} v_{\mathrm{i}}, v_{\mathrm{o}} \in [\dot{m}_{\min}, \dot{m}_{\max}], \quad & v_{\mathrm{i}} + v_{\mathrm{o}} \in [\dot{m}_{\mathrm{t,min}}, \dot{m}_{\mathrm{t,max}}], \\ |v_{\mathrm{i}} - \dot{m}_{\mathrm{sp,i},k-1}| \le \Delta \dot{m}_{\max}, \quad & |v_{\mathrm{o}} - \dot{m}_{\mathrm{sp,o},k-1}| \le \Delta \dot{m}_{\max}, \end{aligned} \tag{34}$$

where $\dot{m}_{\min}, \dot{m}_{\max} > 0$ denote the minimum and maximum air mass flow rates per swirler, $\dot{m}_{\mathrm{t,min}}, \dot{m}_{\mathrm{t,max}} > 0$ denote the minimum and maximum total air mass flow rates, and $\Delta \dot{m}_{\max} > 0$ denotes the maximum magnitude mass flow rate change of air per swirler between steps. At each adaptive controller step, the gradient projection algorithm shown in Section 5.4 in Kelley (1999) is used to solve (33)–(34). Then, the constrained input of the QSRCAC block is given by

$$u_{\mathrm{c},k-1} \overset{\Delta}{=} \dot{m}_{\mathrm{sp},k-1} - \overline{u}. \tag{35}$$

For all $t \in [k\tau_{\mathrm{s}}, (k+1)\tau_{\mathrm{s}})$, the DISCo simulation model input is given by

$$\dot{m}_{\mathrm{sp}}(t) = \dot{m}_{\mathrm{sp},k}. \tag{36}$$

The Cost Function Evaluation block computes J_{k-1} from the sensor measurements. Let $\hat{p}'_{\mathrm{rms}} > 0$ be the RMS of $\hat{p}'$ and let l_{rms} be the number of samples used to compute the RMS as defined in Section 4, such that, for all $t \ge l_{\mathrm{rms}}\tau_{\mathrm{s}}/2000$,

$$\hat{p}'_{\text{rms}}(t) \triangleq \sqrt{\frac{1}{l_{\text{rms}}} \sum_{\kappa=0}^{l_{\text{rms}}} \left[\hat{p}'\left(t - \kappa \frac{\tau_{\text{s}}}{2000}\right)\right]^2}, \tag{37}$$

Hence, for the TISO tests ($l_{\text{z}} = 1$),

$$J_{k-1} = K_1 \hat{p}'_{\text{rms}}(k\tau_{\text{s}}), \tag{38}$$

and, for the TITO tests ($l_{\text{z}} = 2$),

$$J_{k-1} = \begin{bmatrix} K_1 \ \hat{p}'_{\text{rms}}(k\tau_{\text{s}}) \\ K_2 \ \left(\hat{T}(k\tau_{\text{s}}) - \hat{T}_{\text{ref}}\right)^2 \end{bmatrix}, \tag{39}$$

where $K_1, K_2 > 0$, and $\hat{T}_{\text{ref}} > 0$ is the normalized temperature reference value that determines the commanded combustor-exit temperature in the TITO tests. QSRCAC meets the objectives mentioned in Section 4 by minimizing all components of J_{k-1}. Note that the hyperparameters required by the cost function are l_{rms}, K_1, and K_2.

Next, the configuration of the numerical simulations is discussed. The chosen simulation scenarios emulate experiments in which $\dot{m}_{\text{f}} \equiv 0.4$ g/s, $\dot{m}_{\text{i}}(0) = 3$ g/s, $\dot{m}_{\text{o}}(0) = 5$ g/s, and, for the TITO case, $T_{\text{ref}} = 1500$ K; the corresponding simulation parameter values are given by $\overline{u} = [3 \ 5]^T$, and $\hat{T}_{\text{ref}} = 3.7$, which reflects the thermocouple voltage measurement equivalent to approximately 1500 K. Furthermore, the value of τ_{rms} is chosen to properly sample the pressure oscillations, the value of τ_{s} is chosen to approximately match the rise time corresponding to the actuator step response, the values of $\dot{m}_{\text{min}}$, $\dot{m}_{\text{max}}$, $\dot{m}_{\text{t,min}}$, and $\dot{m}_{\text{t,max}}$ are determined from the constraints in Table 1, and $\Delta\dot{m}_{\text{max}}$ is determined from experimental results to prevent flameout; these parameters are shown in Table 3. Figure 9 shows the output values of $\mathcal{F}$, $\mathcal{G}$, and $\overline{\mathcal{G}}$ for all $\dot{m}_{\text{i}}, \dot{m}_{\text{o}} \in [1, 9]$ g/s and the convex constraints given by (34) and Table 3, where $\overline{\mathcal{G}}(\dot{m}) \triangleq |\mathcal{G}(\dot{m}) - \hat{T}_{\text{ref}}|$. For the TISO test, the objective is to reach values of $\dot{m}_{\text{i}}$ and $\dot{m}_{\text{o}}$ that minimize $\mathcal{F}$ within the mass flow rate constraints. For the TITO test, the objective is to reach values of $\dot{m}_{\text{i}}$ and $\dot{m}_{\text{o}}$ that minimize $\mathcal{F}$ and $\overline{\mathcal{G}}$ within the mass flow rate constraints. The perturbation signal function $\mathcal{H}$ used in Mode 2 of QSRCAC is given by

$$\mathcal{H}(k) = [\text{Tr}(k+2) \ \text{Tr}(k)]^T, \tag{40}$$

where $\text{Tr} : [0, \ldots, \infty) \to \mathbb{R}$ is the triangular function

$$\text{Tr}(k) \triangleq \frac{4\alpha}{\beta} \left| \left(\left(k\tau_{\text{s}} - \frac{\beta}{4}\right) \text{mod } \beta \right) - \frac{\beta}{2} \right| - \alpha, \tag{41}$$

where $\alpha = 0.25$ and $\beta = 1.6$ are the amplitude and period in seconds of the triangular function, respectively, and mod is the Euclidean modulo operator, as described in Boute (1992); the triangular function is used in the present work to provide equally-spaced mass

Table 3. Constraint enforcement parameters and controller sampling periods for sampled-data implementation of QSRCAC.

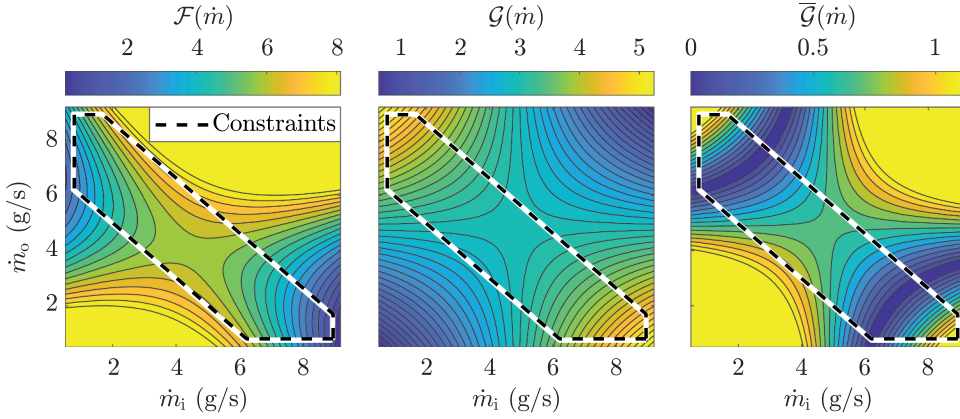|	Constraint Enforcement					Sampling Periods	
Parameter	$\dot{m}_{\text{min}}$	$\dot{m}_{\text{max}}$	$\dot{m}_{\text{t,min}}$	$\dot{m}_{\text{t,max}}$	$\Delta\dot{m}_{\text{max}}$	τ_{rms}	τ_{s}
Unit	g/s	g/s	g/s	g/s	g/s/step	s/step	s/step
Value	0.75	9	7	11.3	0.5	10^{-4}	0.2

Figure 9. $\mathcal{F}(\dot{m}), \mathcal{G}(\dot{m})$, and $\overline{\mathcal{G}}(\dot{m}) \triangleq |\mathcal{G}(\dot{m}) - \hat{T}_{ref}|$ output values with $\hat{T}_{ref} = 3.7$ and $\dot{m} = [\dot{m}_i \ \dot{m}_o]^T \in [1, 9] \times [1, 9]$ g/s. The black, dashed line segments represent the constraints on $\dot{m}_i$ and $\dot{m}_o$. for visualization, the values corresponding to $\mathcal{F}(\dot{m}) > 8.2$ and $\overline{\mathcal{G}}(\dot{m}) > 1.2$ are saturated at 8.2 and 1.2, respectively.
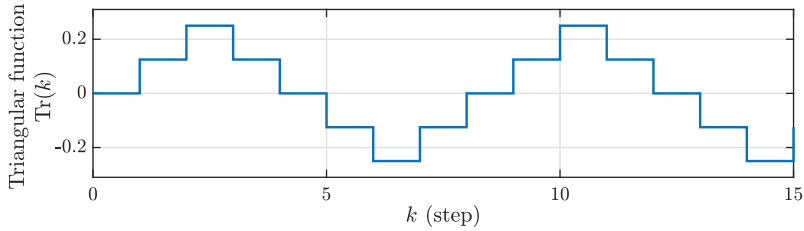
Figure 10. Plot of triangular function $\mathrm{Tr}(k)$ for all $k \in [0, 15]$.

Table 4. Selected hyperparameters for QSRCAC based on simulation results.

Parameter	RCAC				KF				Cost Function		
	l_c	r_u	p_0	$p_{1,0}, p_{2,0}$	q_1, q_2	r_1, r_2	k_1	k_2	l_{rms}	K_1	K_2
Value	1	0.35	10^{-2}	10^{-3}	10^{-1}	10^2	2	6	100	2000	5000

flow rate steps, as shown in Figure 10. Since $\mathcal{H}$ has a discrete-time period of $\beta/\tau_s = 8$ steps, the KF delay indices k_1 and k_2 introduced in Subsection 3.2 are chosen to be one quarter and three quarters of this period, as suggested in Gelbert et al. (2012), such that $k_1 = 2$ and $k_2 = 6$, which is shown in Table 4. QSRCAC initially operates in Mode 1, transitions to Mode 2 at $t = 2$ s, and then transitions to Mode 3 at $t = 12$ s. Hence, the KF is initialized near the initial operating point $\overline{u}$ for 10 s.

Numerical simulation results

Several simulation runs are performed, where the hyperparameters are manually adjusted until QSRCAC yields a value of $\dot{m}$ such that $\mathcal{F}$ is minimized in the TISO test, and $\mathcal{F}$ and $\overline{\mathcal{G}}$ are both minimized in the TITO test. Furthermore, hyperparameters that allow QSRCAC to meet these objectives in the least amount of time are favored to diminish the operating

periods of the combustor, in accordance to the motivation mentioned in Subsection 5.1. The effects of hyperparameter perturbations on the controller's response are discussed in Rahman, Xie, and Bernstein (2017) and studied in a Rijke-tube experiment in Paredes and Bernstein (2023). The selected hyperparameters are shown in Table 4.

The results of the numerical simulations corresponding to the selected hyperparameters are shown in Figures 11, 12 , 13 , and 14 for the TISO test and in Figures 15, 16 , 17 , and 18 for the TITO test. In particular, Figures 11, 14 , 16 and 18 show how the filter coefficient matrix N_k changes with the cost function values represented by $\mathcal{F}$ and $\overline{\mathcal{G}}$, and Figures 13, 14 , 17 and 18 show how the elements of N_k affect the response of QSRCAC and the resulting $\dot{m}_{\mathrm{sp}}$ trajectory. Furthermore, Figures 11 and 15 show that QSRCAC yields air mass-flow rates $\dot{m}$ that locally minimize $\mathcal{F}$ and $\overline{\mathcal{G}}$ in both the TISO and the TITO tests in less than 50 s. Hence, the hyperparameters used in these numerical simulations are used in the laboratory experiments in Section 6.
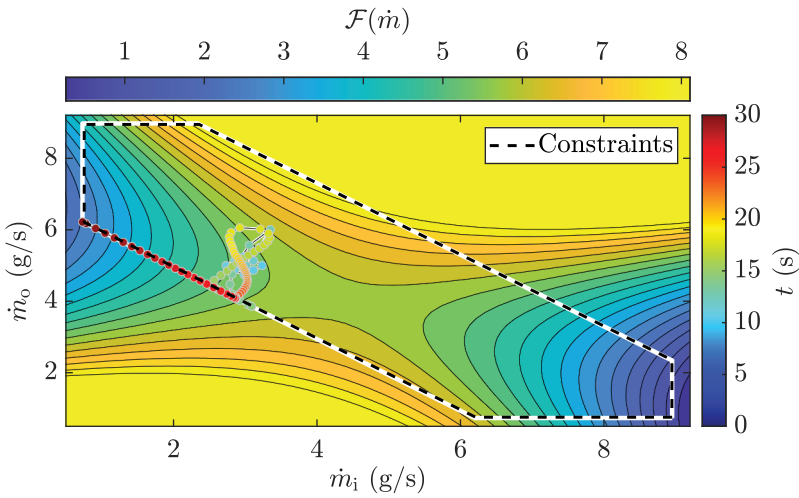
Figure 11. *TISO test*: Evolution of $\dot{m}$ during the closed-loop numerical simulation for $t \in [0, 30]$ s. The output values of $\mathcal{F}(\dot{m})$ for all $\dot{m} = [\dot{m}_{\mathrm{i}} \quad \dot{m}_{\mathrm{o}}]^T \in [1, 9] \times [1, 9]$ g/s are shown in the background. The black, dashed line segments represent the constraints on $\dot{m}_{\mathrm{i}}$ and $\dot{m}_{\mathrm{o}}$.
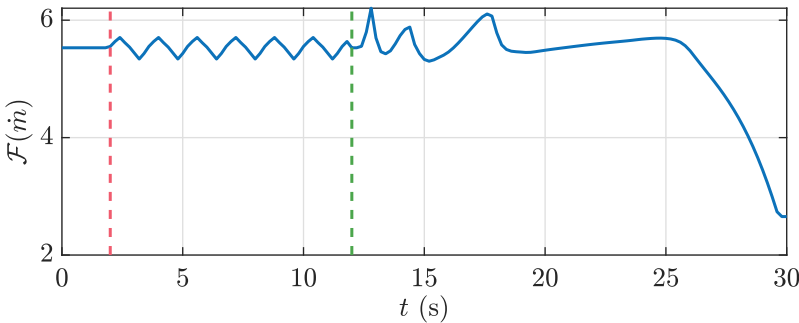

Figure 12. *TISO test*: $\mathcal{F}(\dot{m})$ versus time for the closed-loop numerical simulation. The transitions from Mode 1 to Mode 2 and from Mode 2 to Mode 3 are indicated by the dashed, vertical, red and green lines, respectively.
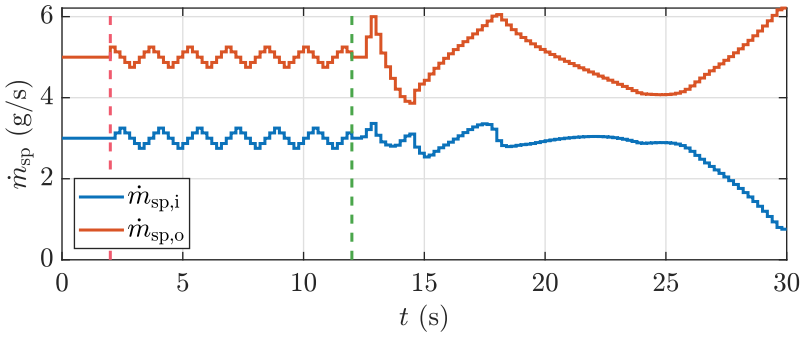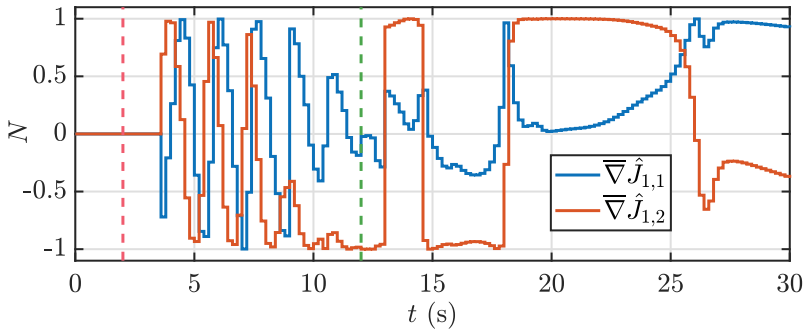
Figure 13. *TISO test*: $\dot{m}_{sp}$ versus time for the closed-loop numerical simulation. The transitions from Mode 1 to Mode 2 and from Mode 2 to Mode 3 are indicated by the dashed, vertical, red and yellow lines, respectively.

Figure 14. *TISO test*: Nonzero elements of filter coefficient matrix *N*, as defined in (24), versus time for the closed-loop numerical simulation. All shown elements are associated with $\mathcal{F}$. Note that $\overline{\nabla}\hat{J}_{1,1}$ is associated with $\dot{m}_{sp,i}$, and $\overline{\nabla}\hat{J}_{1,2}$ is associated with $\dot{m}_{sp,o}$. The transitions from Mode 1 to Mode 2 and from Mode 2 to Mode 3 are indicated by the dashed, vertical, red and yellow lines, respectively.

DISCo laboratory experiments

The DISCo laboratory experiments performed with QSRCAC using the hyperparameters selected in Section 5 are presented in this section. Subsection 6.1 describes the implementation and configuration of QSRCAC with the DISCo facility for experimental tests. Subsection 6.2 presents experimental results. Subsection 6.3 presents a discussion of the results presented in Subsection 6.2.

Sampled-data implementation and configuration of QSRCAC for DISCo laboratory experiments

Figure 19 shows the block diagram of the sampled-data, closed-loop system considered for DISCo laboratory experiments. The implementation is similar to the one described in Subsection 5.2 and shown in Figure 8. The main difference is the output of the Digital Computer block, which is the analog voltage signal vector $V \in \mathbb{R}^{l_u}$ used to modulate the
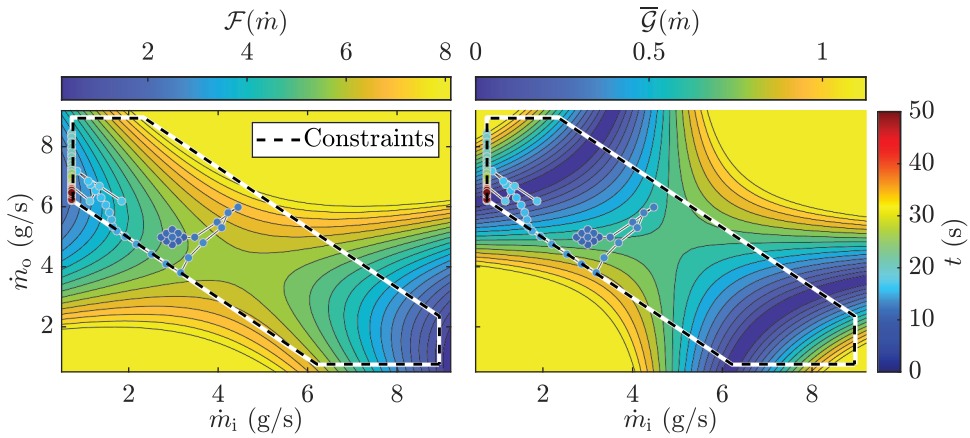
Figure 15. *TITO test*: Evolution of $\dot{m}$ during the closed-loop numerical simulation for $t \in [0, 50]$ s. The output values of $\mathcal{F}(\dot{m})$ and $\overline{\mathcal{G}}(\dot{m})$ with $\hat{T}_{\text{ref}} = 3.7$ and for all $\dot{m} = [\dot{m}_i \quad \dot{m}_o]^T \in [1, 9] \times [1, 9]$ g/s are shown in the background. The black, dashed line segments represent the constraints on $\dot{m}_i$ and $\dot{m}_o$.
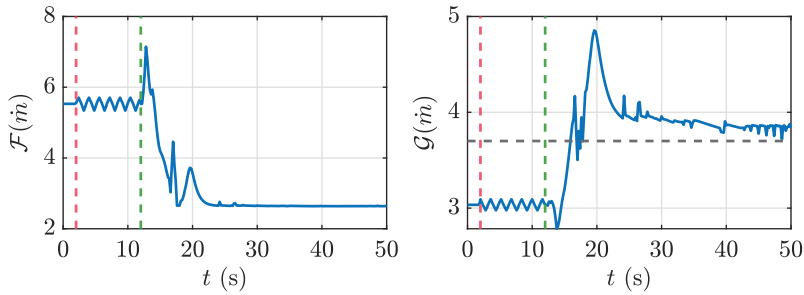

Figure 16. *TITO test*: $\mathcal{F}(\dot{m})$ and $\mathcal{G}(\dot{m})$ versus time for the closed-loop numerical simulation. The transitions from Mode 1 to Mode 2 and from Mode 2 to Mode 3 are indicated by the dashed, vertical, red and green lines, respectively. In $\mathcal{G}(\dot{m})$ plot, the value of $\hat{T}_{\text{ref}}$ is indicated by the dashed, horizontal black line.
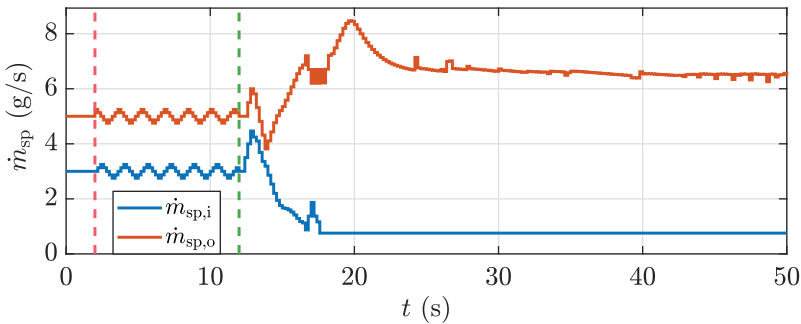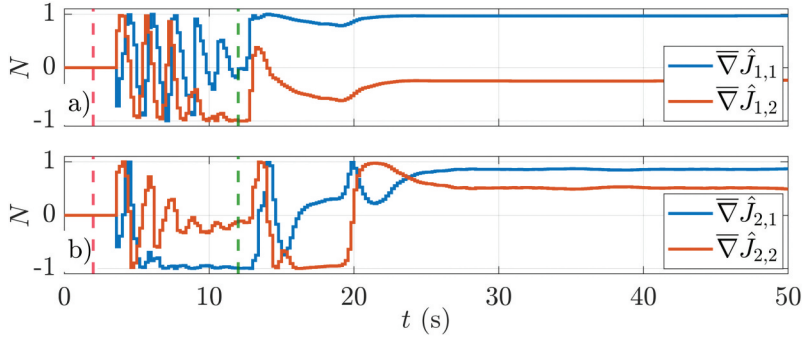

Figure 17. *TITO test*: $\dot{m}_{\text{sp}}$ versus time for the closed-loop numerical simulation. The transitions from Mode 1 to Mode 2 and from Mode 2 to Mode 3 are indicated by the dashed, vertical, red and yellow lines, respectively.

Figure 18. *TITO test*: Nonzero elements of filter coefficient matrix *N*, as defined in (24), versus time for the closed-loop numerical simulation. a) shows the elements associated with $\mathcal{F}$ and b) shows the elements associated with $\overline{\mathcal{G}}$. note that $\overline{\nabla}\hat{J}_{1,1}$ and $\overline{\nabla}\hat{J}_{2,1}$ are associated with $\dot{m}_{\mathrm{sp,i}}$, and $\overline{\nabla}\hat{J}_{1,2}$ and $\overline{\nabla}\hat{J}_{2,2}$ are associated with $\dot{m}_{\mathrm{sp,o}}$. the transitions from Mode 1 to Mode 2 and from Mode 2 to Mode 3 are indicated by the dashed, vertical, red and yellow lines, respectively.
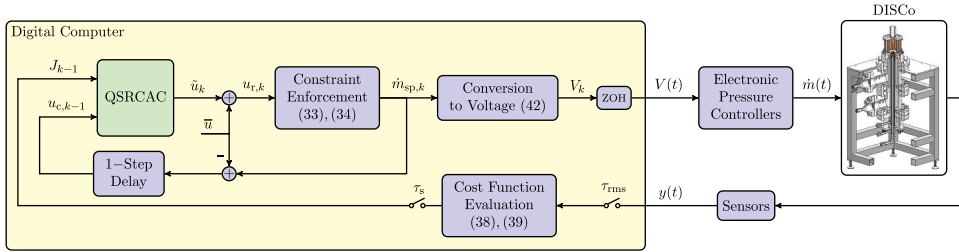

Figure 19. Hardware interconnection of QSRCAC with DISCo.

Electronic Pressure Controllers, such that in steady state $f(V) = \dot{m}$, where $f : \mathbb{R}^{l_{\mathrm{u}}} \to \mathbb{R}^{l_{\mathrm{u}}}$ is an invertible function that can be determined by calibration. Then, for all $t \in [k\tau_{\mathrm{s}}, (k+1)\tau_{\mathrm{s}})$, $V(t) = V_k$, where $V_k \in \mathbb{R}^{l_{\mathrm{u}}}$ is given by

$$V_k = f^{-1}(\dot{m}_{\mathrm{sp},k}). \tag{42}$$

The QSRCAC, Constraint Enforcement, and Cost Function Evaluation blocks are implemented in the same manner as in the numerical examples in Section 5. Furthermore, the parameters and hyperparameters for the laboratory experiments are identical to the ones shown in Tables 3 and 4, and the perturbation signal function $\mathcal{H}$ used in Mode 2 of QSRCAC is given by (40). The controller initially operates in Mode 1. Once the initial conditions are reached by the MCS and control is given to the SACS, the controller transitions to Mode 2. Finally, after 10 s, the controller transitions to Mode 3. Hence, the KF is initialized around the initial operating point for 10 s, as in the numerical simulations.

Table 5 summarizes the initial conditions for all test cases considered for the TISO and TITO experiments. All initial conditions are chosen to be perturbations of a point of maximum instability, which is the combination of $\dot{m}_{\mathrm{t}}, \phi, R$ that yields the highest p'_{rms} value and corresponds to $\dot{m}_{\mathrm{t}} = 8$ g/s, $\phi = 0.85$ and $R = 1.6$ as determined by the open-loop experiments discussed in Subsection 5.1. For all test cases,

Table 5. Initial conditions and final values for DISCo laboratory experiments.

		Initial Conditions								Final Values					
		$\dot{m}_i(0)$	$\dot{m}_o(0)$	$\dot{m}_f$	$\phi(0)$	$R(0)$	T_{ref}	$p'_{rms}(0)$	$T_{err}(0)$ (K)	$\dot{m}_i(t_{end})$	$\dot{m}_o(t_{end})$	$\phi(t_{end})$	$R(t_{end})$	$p'_{rms}(t_{end})$	$T_{err}(t_{end})$
Unit		g/s	g/s	g/s	–	–	K	kPa	K	g/s	g/s	–	–	kPa	K
TISO	Case 1	3.077	4.923	0.396	0.85	1.6	N/A	0.466	N/A		1.587	0.65	0.18	0.094	N/A
	Case 2			0.419	0.9			0.530		8.948	6.548	0.99	8.67	0.067	
	Case 3			0.372	0.8			0.542		0.755	0.755	0.98	0.13	0.225	
	Case 4	4	4	0.396	0.85	1	N/A	0.518	N/A	5.742	1.500	0.65	0.17	0.112	
TITO	Case 1	3.077	4.923	0.396	0.85	1.6	1200	0.488	291.72	8.948	3.452	0.62	0.45	0.075	149.04
	Case 2						1050	0.465	382.56	7.598	3.465	0.62	0.46	0.102	300.83
	Case 3						1500	0.488	146.62	7.539	6.129	0.99	8.12	0.079	33.54
	Case 4		4	0.396	0.85			0.444	142.67	0.755 / 5.959	0.948	0.99	0.16	0.183	73.82

$\dot{m}_t(0) = \dot{m}_i(0) + \dot{m}_o(0) = 8$ g/s to diminish the dimension of the choice for initial conditions. The initial conditions are explained as follows:

- **TISO**: Initial conditions are chosen by making minor changes in the $\phi(0)$ and $R(0)$ relative to a point of maximum instability to assess the susceptibility of the response of the controller to perturbations.
  - ○ **Case 1**: Point of maximum instability, replicates the TISO simulation test case.
  - ○ **Case 2**: Leaner initial condition (decrease in $\phi(0)$).
  - ○ **Case 3**: Richer initial condition (increase in $\phi(0)$).
  - ○ **Case 4**: Same $\dot{m}_i(0)$ and $\dot{m}_o(0)$ values (decrease in $R(0)$).
- **TITO**: In all of these test cases, a point of maximum instability is chosen as an initial condition and different T_{ref} values are chosen.
  - ○ **Case 1**: T_{ref} lower than $T(0)$.
  - ○ **Case 2**: T_{ref} much lower than $T(0)$.
  - ○ **Case 3**: T_{ref} higher than $T(0)$, replicates the TITO simulation test case.
  - ○ **Case 4**: Same initial conditions as Case 3, QSRCAC reaches different $\dot{m}_i$ and $\dot{m}_o$ final values.

Experimental results

This subsection presents the results from the laboratory experiments described in Subsection 6.1. While their equivalent normalized versions $\hat{p}'$, $\hat{T}$, $\hat{T}_{ref}$, and $\hat{p}'_{rms}$ are used by the controller, p', T, T_{ref}, and p'_{rms} as defined in Section 4 are used in this subsection to assess the performance of QSRCAC in a physically significant manner. Furthermore, let t_{end} be the time at which the experiment of a test case ends, $T_{err}(t) \overset{\Delta}{=} |T(t) - T_{ref}|$ for all $t \in [0, t_{end}]$, $p'_{rms,max} \overset{\Delta}{=} \max_{t \in [0, t_{end}]} p'_{rms}(t)$, and $T_{err,max} \overset{\Delta}{=} \max_{t \in [0, t_{end}]} T_{err}(t)$.

The results of the laboratory experiments are summarized in Table 5 and shown in Figures 20, 21 , and 22 for the TISO tests, and in Figures 23, 24 , 25 , and 26 for the TITO tests. In particular, these results show that QSRCAC yields a reduction in p'_{rms} in all TISO test cases and yields a reduction in p'_{rms} and T_{err} in all TITO test cases, although in certain TITO test cases the reduction in T_{err} is not as significant as the reduction in p'_{rms}. This is further discussed in Subsection 6.3.

Discussion

The results from the single objective TISO experimental test cases are discussed first. As it was mentioned in Section 2, there is a critical value of R for a specific ϕ which leads to a highly compact and unstable flame. In the context of the TISO control problem, any major deviation from this critical value will lead to a broadening of the heat release region, thus creating a time and space lag between different heat release points in the combustion chamber and a reduction in p'_{rms}. Although QSRCAC converges to different values of $\dot{m}(t_{end})$ in each test case, all tests result in a reduction in p'_{rms}. In Case 1, in which the initial conditions correspond to a point of maximum instability and replicate those of the TISO simulation test, QSRCAC yields a lean final operating point by reducing ϕ while reducing R;
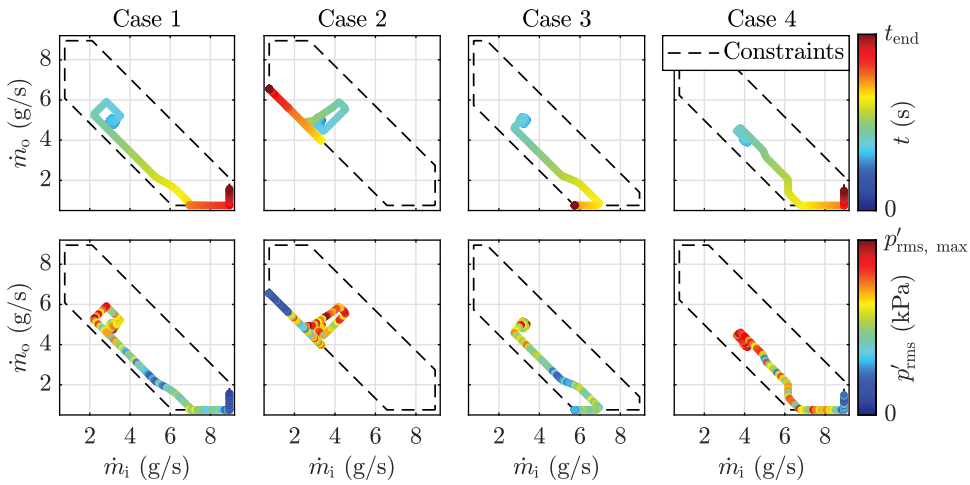
Figure 20. *TISO tests*: Evolution of $\dot{m}$ during each closed-loop laboratory experiment case for $t \in [0, t_{end}]$ s. The p'_{rms} values measured at each $\dot{m}$ point along the trajectory are also displayed. The black, dashed line segments represent the constraints on $\dot{m}_i$ and $\dot{m}_o$.
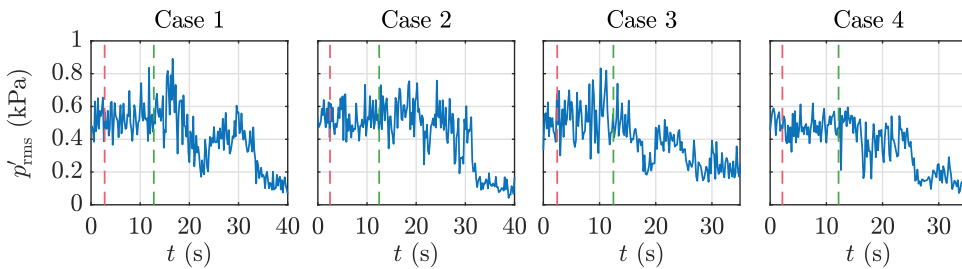

Figure 21. *TISO tests*: p'_{rms} versus time for each closed-loop laboratory experiment case for $t \in [0, t_{end}]$ s. The transitions from Mode 1 to Mode 2 and from Mode 2 to Mode 3 are indicated by the dashed, vertical, red and green lines, respectively.
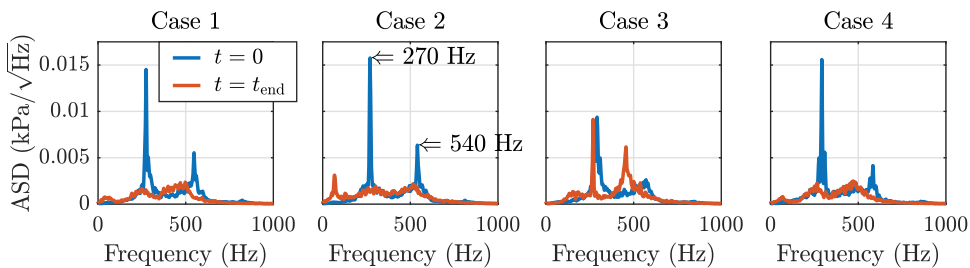
Figure 22. *TISO tests*: ASD of the combustor pressure measurements at $t = 0$ s and $t = t_{end}$ s for each closed-loop laboratory experiment case.
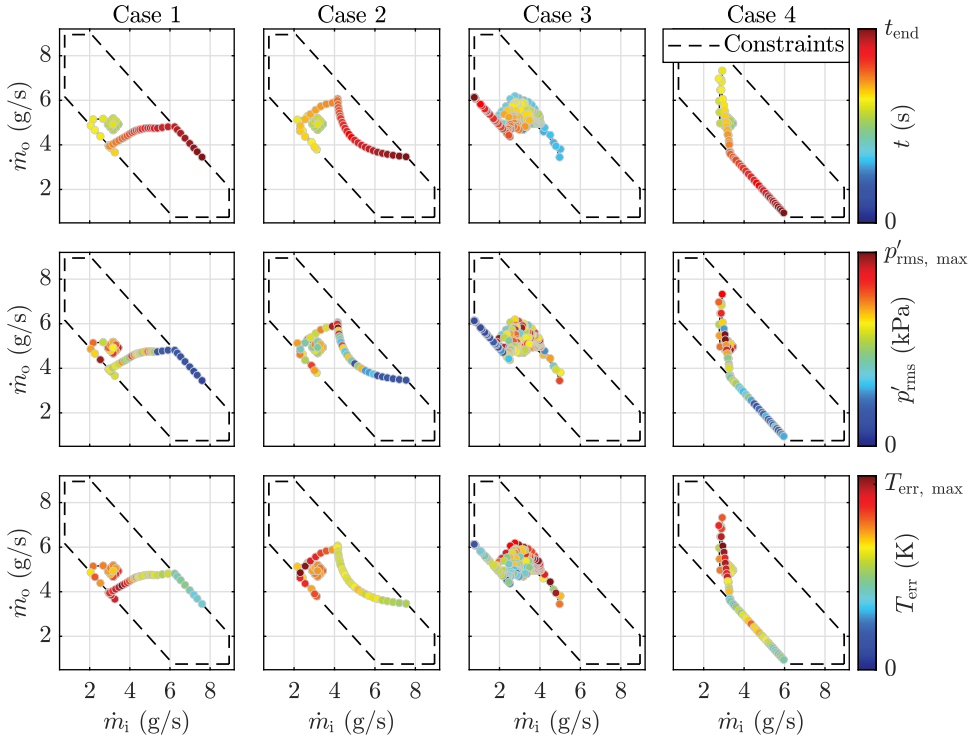
Figure 23. *TITO Tests*: Evolution of $\dot{m}$ during each closed-loop laboratory experiment case for $t \in [0, t_{end}]$ s. The p'_{rms} and the T_{err} values measured at each $\dot{m}$ point along the trajectory are also displayed. The black, dashed line segments represent the constraints on $\dot{m}_i$ and $\dot{m}_o$.
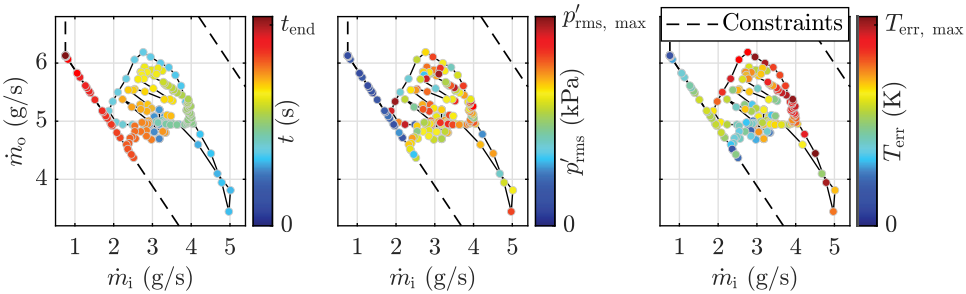

Figure 24. *TITO Test*: Magnified version of the case 3 plots in Figure 23.

while the final operating point of this experimental test is different from the final operating point obtained in its simulation test counterpart, the reduction of p'_{rms} obtained in the experimental test is still significant. The initial conditions of Cases 2 and 3 constitute perturbations in $\phi(0)$ while maintaining the same $R(0)$ relative to the initial conditions of Case 1. In Case 2, in which the initial conditions were chosen to be leaner than those of Case 1 (lower $\phi(0)$), QSRCAC yields a final operating point with higher ϕ while increasing R. In Case 3, in which the initial conditions were chosen to be at higher $\phi(0)$ (but still lean)
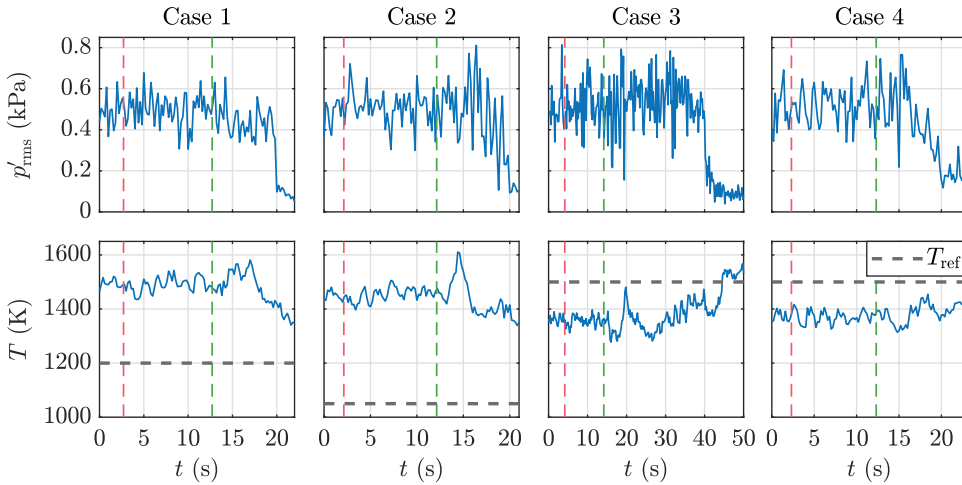
Figure 25. *TITO Tests*: p'_{rms} versus time and T versus time for each closed-loop laboratory experiment case for $t \in [0, t_{end}]$ s. The transitions from Mode 1 to Mode 2 and from Mode 2 to Mode 3 are indicated by the dashed, vertical, red and green lines, respectively. In the plot of T, the value of T_{ref} is indicated by the dashed, horizontal, black line.
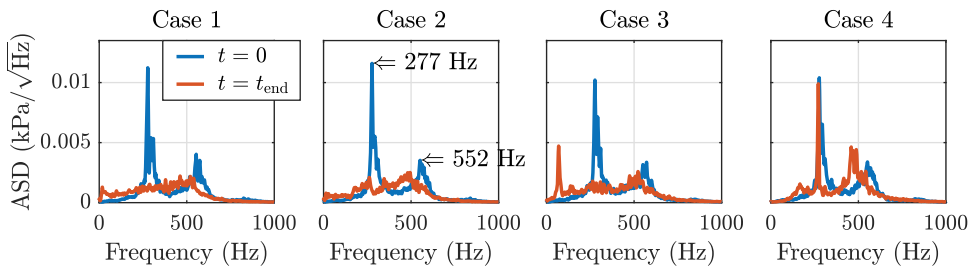

Figure 26. *TITO Tests*: ASD of the combustor pressure measurements at $t = 0$ s and $t = t_{end}$ s for each closed-loop laboratory experiment case.

than those of Case 1, QSRCAC yields a final operating point at higher ϕ while decreasing R. Although the final operating point of this test case yields the least reduction in p'_{rms} out of all cases, it is still a valid solution to the TISO control objective. Unlike Cases 2 and 3, the initial condition of Case 4 constitutes a perturbation in $R(0)$ while maintaining the same $\phi(0)$ relative to the initial conditions of Case 1. In Case 4, in which the initial conditions were chosen to yield a lower $R(0)$ than Case 1, QSRCAC yields a lean final operating point by reducing ϕ while reducing R, similarly to what occurred in Case 1.

The results from the TITO experimental test cases are discussed next. In the context of the TITO control problem, an increase (decrease) in the combustor exit temperature can be obtained by: a) increasing (decreasing) the equivalence ratio implying a change in $\dot{m}_t$ since $\dot{m}_f$ is a constant; b) changing the position and compactness of heat release region by altering R; c) both a) and b). Near the limits of R, the time and space lag between different heat release points in the chamber is increased to the maximum and the objective of decreased p'_{rms} is achieved similar to a TISO test. In such a operating condition, the flame is elongated and has a broad

region of heat release leading to an increase in the firing temperature. Thus, a commanded increase in temperature can be considered a complimentary objective to the objective of decreasing p'_{rms}. Similarly, when a decrease in firing temperature is commanded, a compromise between the two objectives is expected. Thus, a commanded decrease in combustor exit temperature can be considered as a contrasting objective to the objective of decreasing p'_{rms}.

The initial conditions for all the four TITO cases are the same as those of Case 1 of the TISO cases and thus correspond to a point of maximum instability; the temperature goals are modified in each test to determine the response of QSRCAC under contrasting and complementary objectives. Cases 1 and 2 present two contrasting objectives which entail decreasing the p'_{rms} and decreasing the combustor exit temperature. As shown by the results of Cases 1 and 2 in Figure 25, QSRCAC minimizes p'_{rms} with higher priority and yields a distributed flame which limits the reduction of exit temperature. Note that, even though Case 2 features a lower temperature goal than Case 1, QSRCAC reaches a similar operating point at the mass flow rate constraint limit in both cases. Hence, QSRCAC favors the reduction of p'_{rms} and attempts to reduce T_{err} until a limit is reached, thus achieving a compromise between its two contrasting objectives. Cases 3 and 4 present two complementary objectives which entail decreasing the p'_{rms} and increasing the combustor exit temperature. While both cases have the same temperature goal, QSRCAC yields a different operating point in each case; QSRCAC reaches the same equivalence ratio ($\phi(t_{end}) = 0.99$) and opposite split ratios ($R = 8.12$ in Case 3 and $R = 0.16$ in Case 4) in these tests, thus achieving a distributed flame in both cases and meeting the goals satisfactorily.

Figures 22 and 26 show the ASD of the combustor pressure measurements at the beginning and the end of each of the TISO and TITO test cases, respectively. At the beginning of each test case, there exist frequency peaks in the range of 270 Hz and 540 Hz. In Cases 1,2 and 4 of the TISO tests and in Cases 1, 2 and 3 of the TITO cases, the significant peaks in the ASD plots at the beginning of each test are eliminated by the end of each experiment, leading to a broadband noise in the ASD and a significant reduction in the p'_{rms}. However, in Case 3 of the TISO tests and Case 4 of the TITO tests, minor changes in the frequency spectrum between the beginning and the end of the experiment are observed, which corresponds to the lower reduction in p'_{rms} obtained by the final operating points in both cases, which are very similar. Furthermore, note that both Case 2 from the TISO tests and Case 3 from the TITO tests feature a frequency peak in the range of 70 Hz at the end of each experiment which is not associated with the acoustic modes of the combustor elements explored in our previous work Ramesh et al. (2021) and Ramesh and Gamba (2022). In both of these cases, QSRCAC reaches the highest values of ϕ and R allowed by the constraints, which leads to the formation of multiple local hotspots with varying convective delay times in the combustion zone. This in turn causes self-excitation at frequencies that are not correlated to either the longitudinal or Helmholtz mode of the plenums as concluded by Prieur et al. (2017). Experimental DISCo tests not shown in this work reveal that this lower frequency peak shifts slightly in frequency as R is varied near its highest value at the $\phi = 1$ constraint corresponding to $\dot{m}_{t,min}$, while the frequency peaks associated with the plenums Helmholtz modes are more prominent and shift slightly in frequency as R is varied near its highest value at the $\phi = 0.6$ constraint corresponding to $\dot{m}_{t,max}$.
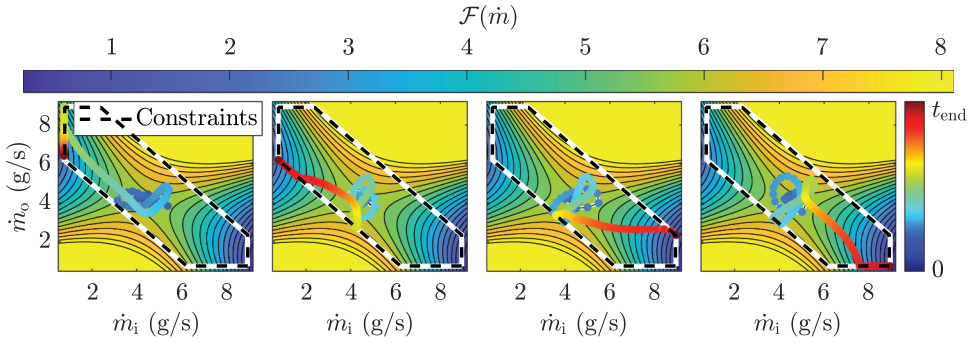
Figure 27. Evolution of $\dot{m}$ during the closed-loop TISO numerical simulations for $t \in [0, t_{end}]$ s, in which $\dot{m}_i(0) = 4.5$ g/s, $\dot{m}_o(0) = 4.2$ g/s, and the $\hat{p}'$ measurement is corrupted by the noise signal w_1, as shown in (32), with standard deviation $\sigma_1 = 1$. each of the plots displays the results under different sequences of w_1. the output values of $\mathcal{F}(\dot{m})$ for all $\dot{m} = [\dot{m}_i \ \dot{m}_o]^T \in [1, 9] \times [1, 9]$ g/s are shown in the background.

In this work, the control problem does not impose that combustor operation to occur at the leanest possible case, but rather, any operating condition with $\phi < 1$ that results in operation with a lower pressure fluctuation than the initial operating state is acceptable. In particular, there exist multiple lean and stoichiometric operating points that minimize p'_{rms} under similar initial conditions, as shown by the results in Subsection 6.2. Hence, reaching either leaner or stoichiometric operating point is acceptable in the present work and QSRCAC is not guaranteed to reach a global minimum. Additionally, since no information on the flame position and structure of the flame is provided to the controller to satisfy the objectives, the controller guides the combustor to operating points in which a single swirler is dominant, which is uncommon in gas turbine operation.

Cases 3 and 4 from the TITO tests show that similar initial conditions can yield different trajectories or final operating points. This is due to the susceptibility to measurement noise of QSRCAC given the chosen hyperparameters. In a highly unsteady environment like a combustor, the operating point trajectory followed by the controller may be influenced by the local state (i.e., p'_{rms}) and the integrated effect of the unsteadiness along the trajectory followed by the controller. Figure 27 illustrates this by showing that QSRCAC can yield different trajectories under the same initial conditions and increased noise standard deviation (10 times greater than the value shown in Table 2). While a different set of hyperparameters may be chosen to decrease susceptibility to measurement noise, this can also decrease the rate of adaptation and estimation of RCAC and the KF, respectively, thus increasing the required operation time of the combustor. Hence, a tradeoff between susceptibility to measurement noise and speed of operation must be chosen when using QSRCAC.

Conclusions

This work developed the following:

- QSRCAC, a quasi-static adaptive controller, for minimizing thermoacoustic oscilla-
  tions and maintaining a user-defined temperature at the exit of the combustor in

a laboratory-scale model combustor in the case where the actuators have low bandwidth relative to the dynamics of the combustor.

- An empirical DOE-based simulation model of the combustor to enable a low-resource hyperparameter selection process, in which the QSRCAC hyperparameters were manually adjusted over several closed-loop simulation runs to determine hyperparameter values that reduce the RMS of the thermoacoustic oscillations and the error between the exit combustor temperature and a reference value.

The selected hyperparameters obtained from closed-loop simulations using the DOE-based model were then used by QSRCAC in laboratory experiments with a gas turbine model combustor. The results of the laboratory experiments were as follows:

- A decrease in thermoacoustic oscillations and temperature error was observed in all studied cases.
- In the TITO cases, when complementary objectives were presented, such as minimizing thermoacoustic instabilities and increasing the exit temperature, QSRCAC achieved both objectives.
- In the TITO cases, when presented with multiple contrasting objectives, such as minimizing thermoacoustic instabilities and diminishing the exit temperature, QSRCAC minimized thermoacoustic oscillations with higher priority.

Acknowledgements

Disclosure statement

No potential conflict of interest was reported by the author(s).

Funding

References

Aarabi, E., M. Ghadiri-Modarres, and M. Mojiri. 2023. Adaptive backstepping stabilization of thermoacoustic instability in a linearized ODE-PDE Rijke tube model. *IEEE. Access* 11:121766–85. doi:10.1109/ACCESS.2023.3329055.

Annaswamy, A. M., and A. F. Ghoniem. 2002. Active control of combustion instability: Theory and practice. *IEEE Contr. Sys. Mag.* 22 (6):37–54.

Boute, R. T. 1992. The Euclidean definition of the functions div and mod. *Trans. Prog. Lang. Sys.* 14 (2):127–44. doi:10.1145/128861.128862.

Bruce, A. L., N. Mohseni, A. Goel, and D. S. Bernstein. 2020. Adaptive quasi-static control of multistable systems. In *Proc. Amer. Contr. Conf.*, Denver, CO (pp. 2055–60).

Brunton, S. L., and B. R. Noack. 2015. Closed-loop turbulence control: Progress and challenges. *Appl. Mech. Rev.* 67 (5):5. doi:10.1115/1.4031175.

Chen, X., H. Fathy, and J. O'Connor. 2020. Impact of sensor placement on mode observability and LQG control of a thermoacoustic system. *IFAC-PapersOnLine* 53 (2):4214–21. doi:10.1016/j.ifacol.2020.12.2466.

de Andrade, G. A., R. Vazquez, and D. J. Pagano. 2017. Boundary control of a Rijke tube using irrational transfer functions with experimental validation. In *Proc. IFAC World Congress*, Toulouse, France (pp. 4528–33).

DeLoach, R. 2000. The modern design of experiments: A technical and marketing framework. In *Proc. Aerodynam. Meas. Tech. Ground Test. Conf.*, Denver, CO (pp. 2691).

Deshmukh, N. N., and S. Sharma. 2017. Suppression of thermo-acoustic instability using air injection in horizontal Rijke tube. *J. Energy Inst.* 90 (3):485–95. doi:10.1016/j.joei.2016.03.001.

Ding, Y., D. Durox, N. Darabiha, and T. Schuller. 2019. Chemiluminescence based operating point control of domestic gas boilers with variable natural gas composition. *Appl. Therm. Eng.* 149:1052–60. doi:10.1016/j.applthermaleng.2018.12.106.

Docquier, N., and S. Candel. 2002. Combustion control and sensors: A review. *Prog. Energy Comb. Sci.* 28 (2):107–50. doi:10.1016/S0360-1285(01)00009-0.

Docquier, N., F. Lacas, and S. Candel. 2002. Closed-loop equivalence ratio control of premixed combustors using spectrally resolved chemiluminescence measurements. *Proc. Comb. Inst.* 29 (1):139–45. doi:10.1016/S1540-7489(02)80022-0.

Dowling, A. P., and A. S. Morgans. 2005a. Feedback control of combustion oscillations. *Ann. Rev. Fluid Mech.* 37 (1):151–82. doi:10.1146/annurev.fluid.36.050802.122038.

Dowling, A. P., and A. S. Morgans. 2005b. Feedback control of combustion oscillations. *Ann. Rev. Fluid Mech.* 37 (1):151–82. doi:10.1146/annurev.fluid.36.050802.122038.

Feitelberg, A. S., and M. A. Lacey. 1998. The GE rich-quench-lean gas turbine combustor. *J. Eng. Gas Turbines Power* 120 (3):502. doi:10.1115/1.2818173.

Gelbert, G., J. P. Moeck, C. O. Paschereit, and R. King. 2012. Advanced algorithms for gradient estimation in one- and two-parameter extremum seeking controllers. *J. Proc. Contr.* 22 (4):700–09. doi:10.1016/j.jprocont.2012.01.022.

Guan, Y., V. Gupta, K. Kashinath, and L. K. B. Li. 2019. Open-loop control of periodic thermo-acoustic oscillations: Experiments and low-order modelling in a synchronization framework. *Proc. Comb. Inst.* 37 (4):5315–23. doi:10.1016/j.proci.2018.07.077.

Gupta, A. K. 1997. Gas turbine combustion: Prospects and challenges. *Energy Convers. Manag.* 38 (10–13):1311–18. doi:10.1016/S0196-8904(96)00160-4.

Gysling, D. L., G. S. Copeland, D. C. McCormick, and W. M. Proscia. 1999, October. Combustion system damping augmentation with Helmholtz resonators. *J. Eng. Gas Turbines Power* 122 (2):269–74. doi:10.1115/1.483205.

Hathout, J. P., M. Fleifil, A. M. Annaswamy, and A. F. Ghoniem. 2002. Combustion instability active control using periodic fuel injection. *J. Prop. Power* 18 (2):390–99. doi:10.2514/2.5947.

Heckl, M. A. 1988. Active control of the noise from a Rijke tube. *J. Sound Vib.* 124 (1):117–33. doi:10.1016/S0022-460X(88)81408-1.

Islam, S. A. U., and D. S. Bernstein. 2019. Recursive least squares for real-time implementation [Lecture Notes]. *IEEE Contr. Sys. Mag.* 39 (3):82–85. doi:10.1109/MCS.2019.2900788.

Islam, S. A. U., T. Nguyen, I. Kolmanovsky, and D. S. Bernstein. 2021, October. Data-driven retrospective cost adaptive control for flight control applications. *J. Guid. Contr. Dyn.* 44(10):1732–58. doi:10.2514/1.G005778.

Keller, J. J. 1995. Thermoacoustic oscillations in combustion chambers of gas turbines. *AIAA J.* 33 (12):2280–87. doi:10.2514/3.12980.

Kelley, C. T. 1999. Simple bound constraints. In *Iterative methods for optimization* Hyman, J. M., 87–108. Philadelphia, PA: SIAM.

Krishnamoorthy, D., and S. Skogestad. 2022. Real-time optimization as a feedback control problem – a review. *Comput. Chem. Eng.* 161:107723. doi:10.1016/j.compchemeng.2022.107723.

Lieuwen, T. C. 2003. Modeling premixed combustion-acoustic wave interactions: A review. *J. Prop. Power* 19 (5):765–81. doi:10.2514/2.6193.

Lieuwen, T. C. 2012. *Unsteady combustor physics.* New York, NY: Cambridge University Press.

Ljung, L., and T. Soderstrom. 1983. *Theory and practice of recursive identification*. Cambridge, MA: The MIT Press.

McDonell, V. 2016. Lean combustion in gas turbines. In *Lean combustion: Technology and control* Dunn-Rankin, D., Therkelsen, P., 147–201. Amsterdam, Netherlands: Elsevier.

McManus, K. R., T. Poinsot, and S. M. Candel. 1993. A review of active control of combustion instabilities. *Prog. Energy Comb. Sci.* 19 (1):1–29. doi:10.1016/0360-1285(93)90020-F.

Mongia, H. C., T. J. Held, G. C. Hsiao, and R. P. Pandalai. 2003. Challenges and progress in controlling dynamics in gas turbine combustors. *J. Prop. Power* 19 (5):822–29. doi:10.2514/2.6197.

Pan, W., X. Xu, J. Li, and Y. Guan. 2020. Acoustic damping performance of coupled Helmholtz resonators with a sharable perforated sidewall in the presence of grazing flow. *Aerosp. Sci. Tech.* 99:105573. doi:10.1016/j.ast.2019.105573.

Paredes, J. A., and D. S. Bernstein. 2023. Experimental implementation of retrospective cost adaptive control for suppressing thermoacoustic oscillations in a Rijke tube. *IEEE Trans. Contr. Sys. Tech.* 31 (6):2484–98. doi:10.1109/TCST.2023.3262223.

Paredes, J., S. A. U. Islam, and D. S. Bernstein. 2022. Adaptive stabilization of thermoacoustic oscillations in a Rijke tube. In *Proc. Amer. Contr. Conf.*, Atlanta, GA (pp. 28–33).

Paredes, J., R. Ramesh, S. Obidov, M. Gamba, and D. Bernstein. 2022. Experimental investigation of adaptive feedback control on a dual-swirl-stabilized gas turbine model combustor. In Proc. AIAA SCITECH 2022 Forum, San Diego, CA. 2058.

Prieur, K., D. Durox, T. Schuller, and S. Candel. 2017. A hysteresis phenomenon leading to spinning or standing azimuthal instabilities in an annular combustor. *Comb. Flame* 175:283–91. January. doi:10.1016/j.combustflame.2016.05.021.

Rahman, Y., A. Xie, and D. S. Bernstein. 2017. Retrospective cost adaptive control: Pole placement, frequency response, and connections with LQG control. *IEEE Contr. Sys. Mag.* 37 (5):28–69.

Ramesh, R., and M. Gamba. 2022. Influence of air split ratio effects on combustion instabilities in a dual-swirl gas turbine model combustor using cinematographic PIV and chemiluminescence imaging. In Proc. Int. Symp. Appl. Laser Imag. Tech. Fluid Mech., Lisbon, Portugal.

Ramesh, R., S. Obidov, J. Paredes, D. S. Bernstein, and M. Gamba. 2021. Design and characterization of the dual independent swirl combustor facility (DISCo). In Proc. AIAA Prop. Energy 2021 Forum, Virtual Event. 3479.

Richards, G. A., M. Janus, and E. H. Robey. 1999. Control of flame oscillations with equivalence ratio modulation. *J. Prop. Power* 15 (2):232–40. doi:10.2514/2.5417.

Richards, G. A., D. L. Straub, and E. H. Robey. 2003. Passive control of combustion dynamics in stationary gas turbines. *J. Prop. Power* 19 (5):795–810. doi:10.2514/2.6195.

Samuelsen, S. 2006. Rich burn, quick-mix, lean burn (RQL) combustor. In *The gas turbine handbook* Dennis, R., 227–33. Morgantown, WV: US Department of Energy, Office of Fossil Energy, National Energy Technology Laboratory.

Sohn, C. H., and J. H. Park. 2011, December. A comparative study on acoustic damping induced by half-wave, quarter-wave, and Helmholtz resonators. *Aerosp. Sci. Tech.* 15(8):606–14. doi:10.1016/j.ast.2010.12.004.

Uhm, J. H., and S. Acharya. 2005. Low-bandwidth open-loop control of combustion instability. *Comb. Flame* 142 (4):348–63. doi:10.1016/j.combustflame.2005.03.015.

Uhm, J. H., and S. Acharya. 2006. Role of low-bandwidth open-loop control of combustion instability using a high-momentum air jet—mechanistic details. *Comb. Flame* 147 (1–2):22–31. doi:10.1016/j.combustflame.2006.08.002.

Wei, W., J. Wang, D.-H. Li, M. Zhu, H.-J. Tang, and F.-L. Weng. 2013. Dynamic compensation based adaptive control of thermo-acoustic instabilities in Rijke tube: An experimental validation. *ISA Trans.* 52 (3):450–60. doi:10.1016/j.isatra.2012.12.010.

Yi, T., and E. J. Gutmark. 2007. Dynamics of a high-frequency fuel actuator and its applications for combustion instability control. *J. Eng. Gas Turbine Power* 129 (3):648–54. doi:10.1115/1.2718558 .

Zalluhoglu, U., A. S. Kammer, and N. Olgac. 2016. Delayed feedback control laws for Rijke tube thermoacoustic instability, synthesis, and experimental validation. *IEEE Trans. Contr. Sys. Tech.* 24 (5):1861–68. doi:10.1109/TCST.2015.2512938.

Zhao, D., C. A'barrow, A. S. Morgans, and J. Carrotte. 2009. Acoustic damping of a Helmholtz resonator with an oscillating volume. *AIAA J.* 47 (7):1672–79. doi:10.2514/1.39704.

Zhao, D., E. Gutmark, and A. Reinecke. 2019. Mitigating self-excited flame pulsating and thermoacoustic oscillations using perforated liners. *Sci. Bulletin* 64 (13):941–52. doi:10.1016/j.scib.2019.05.004.

Zhao, D., and X. Y. Li. 2015. A review of acoustic dampers applied to combustion chambers in aerospace industry. *Prog. Aerosp. Sci.* 74:114–30. doi:10.1016/j.paerosci.2014.12.003.

Zhao, D., Z. Lu, H. Zhao, X. Y. Li, B. Wang, and P. Liu. 2018. A review of active control approaches in stabilizing combustion systems in aerospace industry. *Prog. Aerosp. Sci.* 97:35–60. doi:10.1016/j.paerosci.2018.01.002.

Zinn, B. T., and T. C. Lieuwen. 2005. Combustion instabilities: Basic concepts. In *Combustion instabilities in gas turbine engines: Operational experience, fundamental mechanisms, and modeling* Lieuwen, T.C., Yang, V., 3–26. Reston, VA: AIAA.